NONMECHANICAL MULTIZOOM TELESCOPE DESIGN USING A
LIQUID CRYSTAL SPATIAL LIGHT MODULATOR
AND FOCUS-CORRECTION ALGORITHM

THESIS

Eric W. Thompson, Captain, USAF

AFIT/GEO/ENP/08-03

DEPARTMENT OF THE AIR FORCE
AIR UNIVERSITY

AIR FORCE INSTITUTE OF TECHNOLOGY

Wright-Patterson Air Force Base, Ohio

AFIT/GEO/ENP/08-03

Nonmechanical Multizoom Telescope Design Using A Liquid Crystal Spatial Light Modulator and Focus-Correction Algorithm

THESIS

Presented to the Faculty

Department of Electrical and Computer Engineering

Graduate School of Engineering and Management

Air Force Institute of Technology

Air University

Air Education and Training Command

In Partial Fulfillment of the Requirements for the

Degree of Master of Science (Electro-Optics)

Eric W. Thompson, B.S. in Astronomy and Astrophysics

Captain, USAF

March 2008

Nonmechanical Multizoom Telescope Design Using A Liquid Crystal Spatial Light Modulator and Focus-Correction Algorithm

Eric W. Thompson, B.S. in Astronomy and Astrophysics

Captain, USAF

Approved:

/signed/	March 2008
Capt Jason Schmidt, PhD (Chairman)	date
/signed/	March 2008
Dr. Stephen Cain (Member)	date
/signed/	March 2008
Major Timothy Russell, PhD (Member)	date

Abstract

Theoretical development and design of a compact nonmechanical multi-zoom telescope system is presented. A liquid crystal spatial light modulator (LC SLM) enables selection of four seperate beam paths without the use of moving parts. Each path incurs a different focus aberration in the image plane that can be deconvolved with postprocessing to yield four possible corrected magnification options. To increase flexibility, each region has a 40-wave subrange of focus. Optical zooms of up to 10 times magnification are feasible and are limited only by system noise and signal to noise ratio. Elimination of moving parts for focus could prove beneficial for sysems in which weight, volume, and power consumption have stringent requirements. The presented design can be constructed using all commercial off-the-shelf parts.

Acknowledgements

First and foremost, I'd like to thank my cats Rocky and Merlin. Without their ceaseless efforts to knock over everything in sight at all hours of the day and night, I never would have been awake long enough to complete this thesis. I would also like to thank my girlfriend, whose quick wit, youthful exuberance, constant companionship, and ability to use appliances has made my time here enjoyable. And, in loving memory of Stephanie.

Eric W. Thompson

Table of Contents

Page

List of Figures

Nonmechanical Multizoom Telescope Design Using A Liquid Crystal Spatial Light Modulator and Focus-Correction Algorithm

I. Introduction

The emergence of spatial light modulator (SLM) technology combined with telescopes has introduced many new synergistic opportunities. Some of these applications include nonmechanical zoom, increase in field of regard, tilt correction, beam steering, aberration correction, and aberration analysis through image entropy. [1,9,12,15] The ability to accomplish zoom without using a standard double or triple motor cam-driven system makes it a realistic and potentially inexpensive possibility to utilize with any size telescope. Liquid crystal (LC) SLMs are 2-D computer-controlled systems that modulate the phase of light reflecting off a high-density surface. Common LC SLMs have over 260,000 individual elements in less than an eight-milimeter square and are optimally designed for a single wavelength. [12] The research presented here includes a new design for a nonmechanical zoom telescope using a LC SLM as a beam path selector. A proof of concept for achieving large optical zoom without the need for focusing in the image plane is also shown.

1.1 Zoom

The type of zoom specified in this research is known as optical zoom. This is extremely different from digital zoom. A standard personal digital camera will have both options. The difference is that an increase in the optical zoom represents an increase in the spatial resolution across the image. This makes a section of the original image appear closer while maintaining sharpness and clarity. Digital zoom can make the image appear closer as well, but no extra information is collected. This can lead to a blurry, pixelated appearance (see Fig. 1.1). It is important to understand

(a) Normal View   (b) Optical zoom   (c) Digital zoom
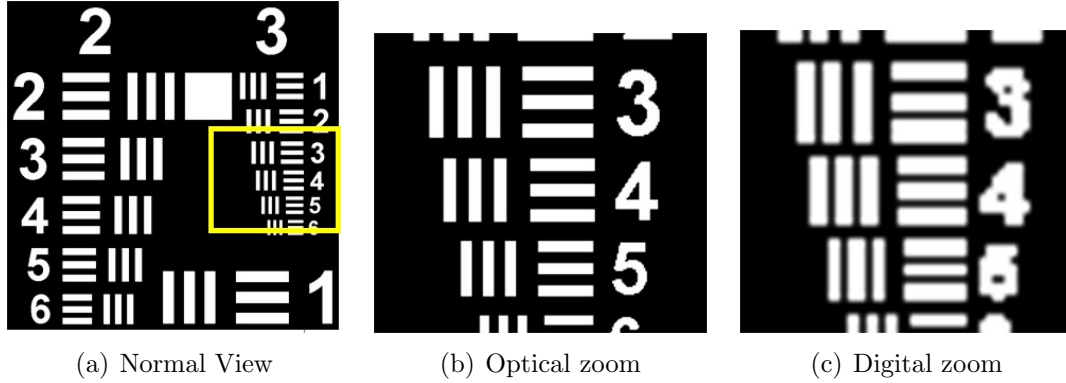
Figure 1.1:   Visual comparison of optical and digital zoom. The square in (a) is zoomed optically in (b) and digitally in (c). The optical zoom makes the section appear closer, but still clear because of the increased spatial resolution. The digital zoom appears blurry because no extra information was obtained.

that the "blur" from the digital zoom is not the same as a blurry image from being out of focus. This is discussed later.

1.2 Mechanical and Nonmechanical Zoom

Mechanical zoom is, by far, the most prevalent means of achieving optical zoom (see Fig. 1.2). For example, it is used for personal cameras, binoculars, microscopes, video cameras, and several imaging telescopes. The mechanism involved is usually a two or three lens moving group with an extra lens to refocus light on the image plane. The lenses in the moving group each require a separate motor. These motors most frequently drive a cam (screw system) to adjust position for each element.

Any nonmechanical system must achieve the same effect, but without the moving groups. There has been progress using optical switches [8] with a Ritchey-Chretien telescope to obtain two magnifications. This however, does not provide a large enough range to be considered a possible replacement for a mechanical system. The research presented here concentrates on a new design capable of providing a large range of zooms nonmechanically.
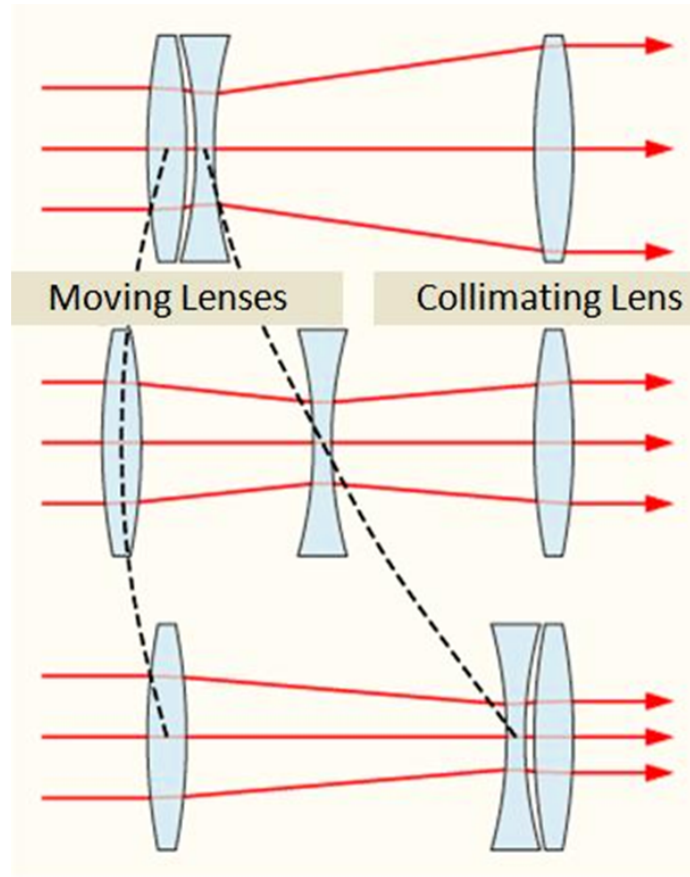
Figure 1.2: This figure illustrates a classic two-lens moving group for mechanical zoom. The position of the two lenses controls the size of the beam when it hits the collimating lens. This results in a larger or smaller collimated beam. A separate focusing element focuses the light onto an image plane. The different beam sizes become different magnifications of the field. As the size of the image in the image plane increases, a higher spatial sampling on the detector is obtained, thus creating a zoom. Figure from *www.wikipedia.com*.

1.3 Liquid Crystal Spatial Light Modulators

To attain nonmechanical zoom, the presented design utilizes a liquid crystal (LC) spatial light modulator (SLM). The LC portion is a uniaxial birefringent (two index) medium that can realize commanded refractive index maps across the device. [1] Since phase velocity is proportional to the index of refraction, the wavefront across the entire device can be manipulated. [16] LC SLMs can be addressed electronically, and therefore easily controlled by a computer. There are types of SLMs that are optically controlled, but this research will focus soley on the electronic. An AC electric field applied across the LC SLM causes a change in the orientation of the optical axis for each small portion, thus imparting a range of optical path differences OPDs across the wavefront. Conrolling the OPDs allows the LC SLM to be used as a programmable diffractive optic (PDO).

1.4 Research Goal and Approach

There are two main goals of this research. First, it must be determined how a nonmechanical, multi-zoom system is theoretically possible. Second, a realistic, practical, and realizable design needs to be created.

To find a theoretical solution, many applications of LC SLMs will be examined in an attempt to ascertain which, if any, can provide nonmechanical zoom. Statistical noise will be incorporated into the theory since real systems have noise.

Once the solution is found, the optical design software CodeV is used to accomplish the second goal. To ensure the system is realistically buildable, only common glasses, coatings, and spherical shapes will be used. The entire setup will be kept small and compact, yet larger versions will still be simple to construct.

Globally, CodeV is the most widely used optical design software. It has been called upon for numerous well-known design problems, such as creating the corrective lenses for the Hubble Space Telescope. CodeV relies on extremely fast ray tracing to allow for computations that can range from seconds, to minutes, to even hours faster

than similar type packages while maintaing the same or better accuracy. A 3.0 GHz Core2Duo processor with 2.0 Gigabytes of DDR2 RAM was used to help speed along calculations. Once a design was created, a detailed analysis of the system aberrations was performed.

The intent of this research is not to provide a fully developed end-use design for nonmechanical zoom. The goal is to create a scalable, constructible, flexible alternative that is capable of synergistic integration with many types of emerging LC SLM technologies.

II. Theory Review

This chapter discusses a variety of concepts central to this research. It starts with the basic idea of a telescope and telescope design. A wide variety of capabilities resulting from combining LC SLMs and telescopes is then presented. Knowledge of these capabilities is paramount since the theory for creating a nonmechanical zoom system was developed to ensure the final design concept could potentially incorporate mutliple emerging technologies. The topics most relevant to this thesis are then discussed.

2.1 Telescopes and Telescope Design

The technology necessary to make a a telescope has been around since the invention of eye glasses in the 1300s. However, it took another 300 years to put a convex and concave lens together appropriately to magnify distant objects and create the first telescope. It cannot be verified who initially put the two lenses together, but Hans Lippershey became noteworthy in 1608 in several parts of Europe. Galileo did not appear on the scene until 1609, and it took him nearly a year longer to point it skyward at night. [10] This type of telescope, understandably, is called a refractor. Small, basic refractors are extremely simple to construct which is why this was the first type built. Binoculars, for example, are simply a pair of refracting telescopes next to each other. Refractors, however, have scalability issues. This was realized in the late 1800s as the 36" Lick, and 40" Yerkes refractors were completed. The immense weight of the optics along with image quality issues ended the growth of this type of telescope. [10]

The reflective telescope became dominant starting in the early 1900s and remains so today. The main reasons for its popularity are the scalability of the optics and the ability to have more compact designs. Single mirror systems currently exist up to 10m in size, while composite systems are planned for over 30m. Even though large reflectors are impressive, smaller systems are much more prevalent. These smaller systems are utilized in many laboratory experiments, imaging systems, and even sim-

(a) Newtonian Focus   (b) Cassegrain Focus   (c) coudè Focus
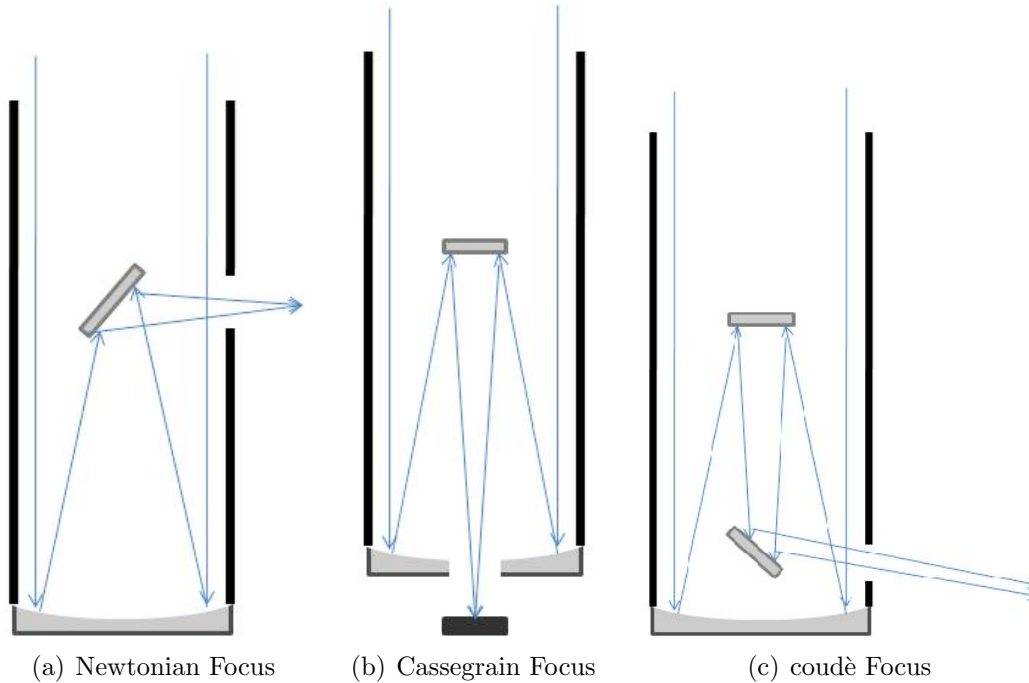
Figure 2.1:   An assortment of focus options are available for reflective telescopes. The location of instrumentation determines the type of focus. A CCD mounted on the back of the primary mirror in (b) would be said to be at the Cassegrain focus. The three types shown here have multiple possible variants.

ple"backyard" telescopes. Reflectors use a central, reflective, obscuration to direct light from the primary to a focus or to another beam path. This obscuration shape can range from flat to a high order conic. Allowing light to travel both directions in the telescope leads to a design much more compact than refractors.

There are large number of design parameters, other than focus location, to consider. A wide variety of standard types of telescopes are available. One of the most common is called a Ritchey-Chretien (RC). A modified RC with coudè focus was chosen to use for the nonmechanical system. The surface figure details and full design will be shown later.
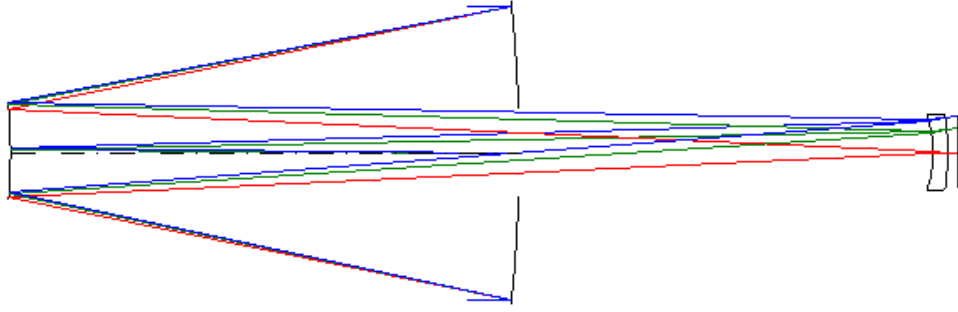
Figure 2.2: A ray trace of a standard RC with Cassegrain focus is shown. This telescope was generated using templates in CodeV. A modified RC with coudè focus has been used for the final nonmechanical system.

2.2 Liquid Crystal Spatial Light Modulator Applications

Many emerging LC SLM technologies can potentially contribute to a nonmechanical zoom system. Some of these applications include increase in field of regard, tilt correction, beam stearing, on-axis and off-axis aberration correction, system analysis through image entropy, and active optical components. Below are descriptions of some of the abilities and drawbacks of using a LC SLM.

2.2.1 Defocus Aberration Correction.

Gruneisen, et al showed that a LC SLM can be used as a PDO capable of compensating for over 40 waves of defocus aberration. [11] The image, a 1951 USAF bar chart, regained near-diffraction-limited resolution after the defocus correction. That represents a factor of 160 increase in the standard quarter-wave Rayleigh diffraction-limited imaging criterion.

An analysis of the system at 532nm showed -0.24 waves of spherical aberration from the primary mirror. Adding 40 waves of defocus creates a challenging problem to correct with a single optic. This however, can also be broken down into Zernike coefficients. Adding these terms creates an overall optical path function that needs to be compensated. It would be expensive and time consuming to obtain a static manufactured optical element capable of correcting this. Depending on the needed

8
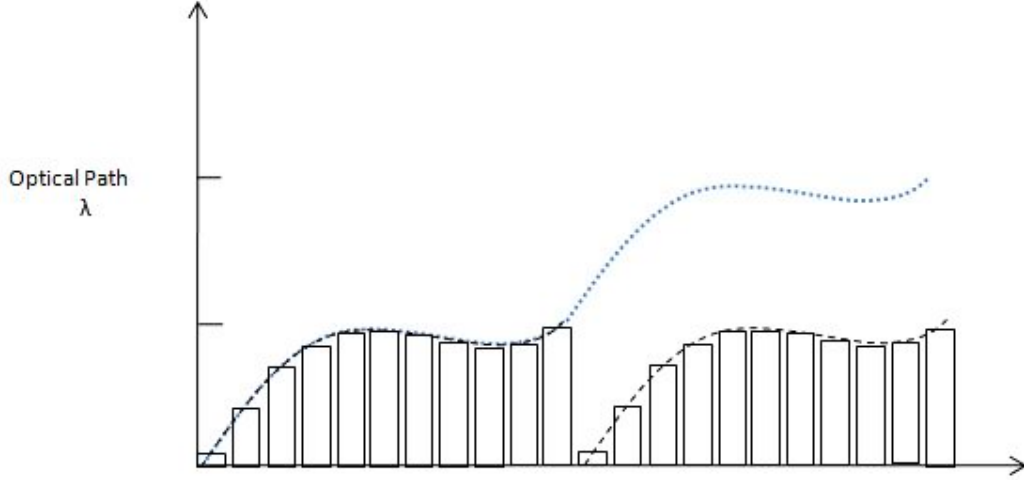
Figure 2.3:   A LC SLM uses individual elements in discrete steps to approximate an optical path function modulo-λ. The dotted line and dashed line are equivalent optical path functions.

optical path function, it may not even be possible to make. A PDO, however, can use a modulo-λ reset to approximate the necessary shape. [11] After applying the expected optical path function, an interferogram revealed the residual aberrations in the system. These were changed to Zernike coefficients and combined with the previous terms. This led to the factor of 160 improvement in depth of focus. Although the focus errors were created by moving the object, the ability to correct for large aberrations using a PDO with modulo-λ will be useful in creating a nonmechanical zoom system.

2.2.2   Increasing Field of Regard.

In general, telescope systems cannot increase their field of regard (FoR) without some form of gimbaling or slewing. Although mechanical movement is highly effective, the requirement for multiple moving drives is not an option for creating nonmechanical zoom. However, SLMs have been used to correct large field angle aberrations while steering the wavefront over angles greater than the instantaneous field of view. [15]

In order to show the dynamic range of field angle aberration correction, a primary mirror was gimbaled 5° relative to the optic axis. This means the view was

centered 10 degrees off the primary mirror's axis. Due to the SLM's wavelength dependence, a spectrally filtered Xenon lamp, centered at 543nm, illuminated a 1951 USAF bar chart. System aberrations included 19.5 waves of astigmatism rotated 1.1° from horizontal, 1.4 waves of coma rotated 11° from horizontal, and -0.3 waves of spherical aberration. [15] Even with the large field angle aberrations, the LC SLM could be controlled to retrieve near-diffraction-limited performance, constituting a factor of 1000 increase in FoR for the system. A more impressive result for this research was the factor of 5 FoR increase using only the steering capability of the LC SLM, while the telescope was not moved at all.

2.2.3   Diffraction Efficiency.

Due to the discrete nature of LC SLMs, light loss from diffraction is a major concern. The jumps between each element (see Fig 2.3) cannot smoothly approximate the necessary optical path. There are options, however, when trying to fit the optical path. Resetting the LC SLM at integer multiples of the reset wavelength yields different diffraction efficiencies. [14] This is known as modulo-$N\lambda_0$ optical path control (see Fig. 2.3). This becomes very important if operating at a wavelength λ that is different from the ideal optical path reset wavelegth λ_0. The higher N becomes, the faster degredation of efficiency occurs as λ_0/λ strays from unity. [14] Both Strehl ratio analysis and Fourier analysis agree for this Nth-order efficiency behavior. The impact on this research is clear: bandpass must be limited to accurately control light from the wavefront.

2.2.4   Wavelength Dependence.

Predictions on the need for a limited bandpass when using a LC SLM must be explored. This, obviously, is quite different than using a deformable mirror (DM) for aberration correction. An adaptive optic (AO) DM uses optical path compensation to correct aberrations in optical systems [19]. This allows for compensation at any wavelength over which the mirror coating is reflective. A LC SLM, however, provides a much higher density of elements. A standard 8" DM could have 941 actuator,

(a) Modulo $1\lambda_0$

(b) Modulo $\lambda_0/2$
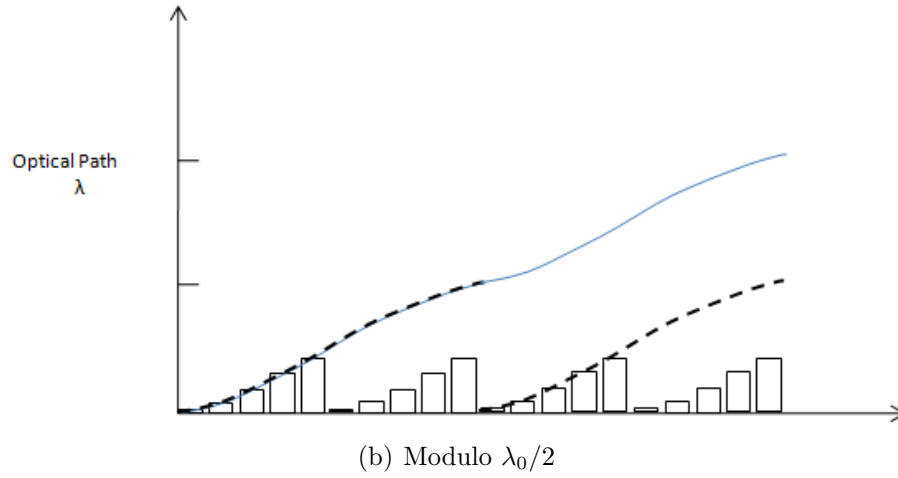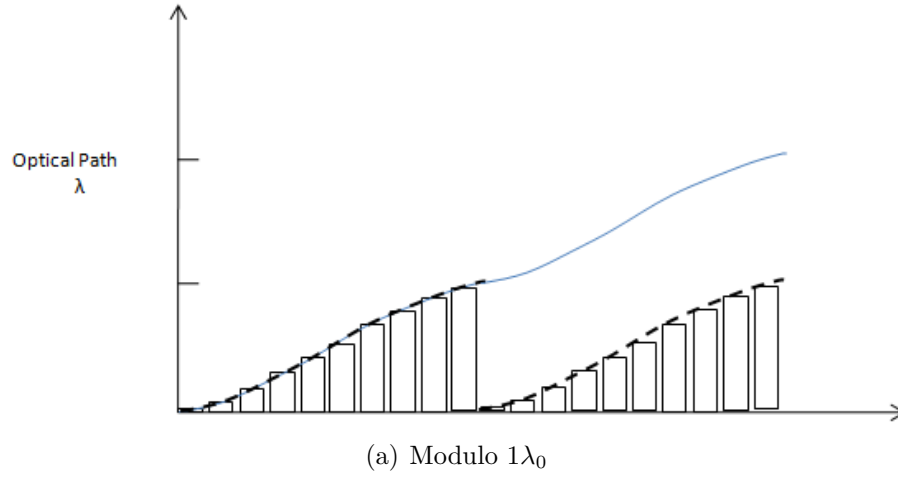
Figure 2.4:   Modulo-$N\lambda_0$ refers to the number of times the LC SLM resets for 1 λ_0 of optical path. Part (a) shows only 1 reset while part (b) shows 2 resets. Theoretically, these two approximations are the same. However, the discrete steps incur varying light losses due to diffraction.

whereas a standard LC SLM could have 262,144 in a 7.62mm square. That means corrective elements in a LC SLM are packed in over 150,000 times more densely than in a DM. This becomes the tradeoff - extreme resolution for limited bandpass.

Analytic solutions have been found and tested for the wavelength dependence of modulo-λ wavefront correction. [13] Note that the corrected image is an incoherent summation of each component in the multi-spectral wavefront. As suggested in the previous section, reset wavelengths were set for the middle of each bandpass. An incoherent xenon lamp with 10, 30, 50, and 100nm bandwidth filters (all centered around 543nm) were used. While high resolution features were still resolvable in the 100nm bandpass, performance doesn't return to near-diffraction-limited until dropping down 10nm. Any nonmechanical zoom telescope built with a LC SLM must therefore operate within specific wavelength ranges to retain near-diffraction resolution of images.

2.2.5   Image Entropy.

Recent developments have shown that LC SLMs can be used in combination with image entropy to increase image quality in the presence of large aberrations. [9] Image entropy is a metric that examines the uniformity of counts per pixel and provides a unique way of measuring the aberrations in a system. The possible advantages are quite numerous. First and foremost, it can eliminate the need for additional calibration hardware in a system. This is extremely important for small designs as it allows for a more compact setup, weighs less, can cost less, and has very low power needs. Components already in the system provide all the necessry information. Not only can the LC SLM measure aberrations in the system, it can then correct for them - all of which is done without moving parts.

This method relies on iterative optimization algorithms that are efficient enough to remain effective even in the presence of large aberrations. This method has already been employed effectively for discerning best focus automatically for solar telescopes. [7] Guidelines for the algorithm have been clearly defined for over a decade. [20] The process is based on the idea that entoropy S for an image with a total number

accounts U in an image is maximized when the PDF of the image becomes uniform. Another way of looking at it is entropy reaches maximum when an even distribution of counts per pixel is achieved. This concept is combined with the fact that there are more possible ways to achieve maximum entropy for a nearly uniform image as opposed to highly non-uniform images. Creating a normalized entropy is necessary to comapre images with different count totals. As aberrations increase, an image loses contrast. This loss of contrast heightens uniformity, which results in a higher entropy and a normalized entropy (S_{norm}) approacing unity. As image"sharpness" increases, S gets smaller and thus S_{norm} decreases as well. Using a LC SLM, this method has been shown to be able to pick out a least aberrated image for up to 20 waves of aberrations in the system. The ability to nonmechanically do system diagnosis and correct up to 20 waves of aberrations for low power consumption, small size, and low cost is of great interest to this research.

2.3 Current Nonmechanical Zoom

The desire for larger, higher detailed images has been around since the invention of the camera. The standard answer of a moving group optical zoom is not satisfactory for all types of applications. There is a wide variety of reasons why this may be the case, and a few possible solutions are examined here. First, the data may already exist, and an increase in resolution is desired. Secondly, adding a zoom to the current system for future data may not be feasible. Lastly, the operating environment may not be conducive to sensitive mechanical parts.

2.3.1 Smart Digital Zoom.

There are many options in imaging processing for sharpening an existing image. One such process, called smart zooming, is rewiewed here. Smart zooming attempts to smooth rough edges left by pixelation from normal digital zooming. [17] By smoothing the pixelated regions, details that were previously unnoticeable can be revealed. The technique uses radial basis function interpolation. The idea that the interpolation uses

circular Gaussian basis functions in such a way that the generated spatial frequency power spectrum usually minimizes the integrated squared deviation from the original data power spectrum. [17, 18]. Smoothing done in this fashion does not change the power spectrum of the original data. Even though this is useful, this step alone cannot compensate for extremely large image aberrations not accomplish a true optical nonmechanical zoom.

2.3.2 Dual Field of View Telescope.

The first attempt at a nonmechanical zoom telescope was patented in 2004. [8]. The design relied on a RC telescope with a large optical switch placed between the primary and secondary mirrors. Turning the switch on or off (transparent or reflective) would create the two different beam paths by reflecting light either off the secondary or the switch. Ideally the switch would be placed so that both paths used the same Cassegrain focus. Reflecting off the switch instead of the secondary would create a larger image in the focal plane, thus creating a zoom. This idea sounds promising, but some extremely important design parameters were not discussed. No mention was given on how to mount and power the switch inside the telescope tube. Any mounting and/or power cables would effect the image. Also, primary and secondary mirrors in a telescope system are designed to minimize system aberrations due to their shapes. It takes both surfaces, with carefully designed constraints, to limit image deformation. Using only the primary and a flat surface would incur aberrations in the image plane. Despite only two fields of view and incomplete design details, the idea that nonmechanical optical zoom is possible was valuable to this research.

2.4 Focus Aberration Estimation

A recent advance in focus aberration estimation has reduces the apparatuses required for error detection. It eliminates the need to split light in the beam path, which results in higher SNR. [3] Another benefit is that this new algorithm produces estimates from a single image. Focus aberration occurs when the detector plane and

image plane are not in the same location. The amount of defocus depends on the separation of the two planes. This type of aberration has a characteristic shape associated with its Zernike mode that changes in magnitude as defocus increases. The genral shape, though, does not change and can be described with a Zernike polynomial. [22] A phase screen, with $\lambda/2\pi$ added for wavelength independent analysis, was used to produce optical transfer functions (OTF) necessary for the deconvolution algorithm to estimate the focus error. [2] This algorithm is used to post-process data from the camera. The core of this procedure revolves around a Richardson-Lucy algorithm. [21] It is very important that the input aberration is known for it to work properly. This may sound like the answer must be known before the work is done, but it is not. This algorithm allows for the retrieval of an object with a known OTF. Knowing what the object is beforehand is not necessary, just the OTF. The process has been shown to accurately estimate up to tens of thousands of waves of focus aberration. Retrieving objects with known focus aberrations, and hence known OTFs, is of great interest for this research.

III. Methodology

This chapter will discuss the basic principles and concepts behind designing the nonmechanical zoom telescope. The mechanisms include nonmechanical beam path selection and focus aberration correction in the image plane. A detailed discussion of the angle selection system and its components will be provided. Verification of a focus correction algorithm will be given along with MATLAB code. An overview of the opical design software, CodeV, will also be included.

3.1 Nonmechanical Beam Path Selection

One of the most difficult pieces of designing a non-mechanical zoom telescope is creating different optical paths for the light to follow. In a standard non-mechanical system, a continuous, bounded range of zooms is available. Although not technically true, each different possible zoom can be thought of as a different optical path. Picturing a standard zoom in this fashion led to the concept of creating separate beam paths for a nonmechanical system. Obviously, a series of beam splitters would present a simple, non-mechanical solution. However, 50 percent of the light would be lost per split. Using only enough splits for four beam paths, only a meager 25 percent of the incoming light would be available for each section. Decreasing the signal by 75 percent to view each zoom would severerly cripple such a system's ability to operate in a low SNR environment. That solution is unacceptable and was the first focus of this research.

The solution for keeping the most possible light in each beam path comes from angle selection using a LC SLM and from a well-designed mirror system. Along with its many other capabilities, as stated in chapter two, LC SLMs allow for a small amount of beam steering. [15] This is done purely by incurring different phase delays across the LC SLM. The beam steering capability, however, is severely limited. The LC SLMs reviewed only cover a +/- 0.1° spread. By itself, this is not enough throw to select separate paths in a compact design (want 2ft cube instead of using up an entire optical bench). To increase the throw of the system, a series of four mirrors

amplifies the initial angular offset. This amplication works for any angular direction chosen. Once the offset is sufficiently increased, a four-sided reflective optical pyramid is used to send light in one of four different directions. (see Fig. 3.1) Each of the four directions becomes a separate beam path, all with much greater than 25 percent of the incoming light. The only light lost is from reflective losses in the mirrors and diffractive losses in the SLM.

3.2 Focus Aberration Correction

This section delves into the specifics of how to create different magnifications (zooms) on the image plane. Since this is a compact design, the number of optics and their complexities must be taken into consideration. Ideally, a single spherical mirror along each beam path could impart a different focus for the light. Creating a different focus for each path changes the height of the chief ray in the image plane, thus imparting an optical zoom. The quandry becomes how in the design to account for non-converging marginal rays in the image plane. The answer actually was very simple - do not do it. The goal of this section is to examine the relationship between SNR, focus error, and image deconvolution, and to explain how this actually creates an optical zoom in need of post-processing.

3.2.1 Source of Focus Aberrations.

Several factors can contribute to focus abberation in the image plane. Other aberrations in a system such as spherical or astigmatism can create a "best focus" plane which may or may not coincide with the image plane. Although this can lead to focus error in the image, it is not large enough to be investigated here. The largest source simply comes from the focal plane being displaced from the image plane. The actual location of focus for a simple system is governed by the thin lens equation. [6] This equation uses s_o for object distance, s_i for image distance, and f for the focal length.
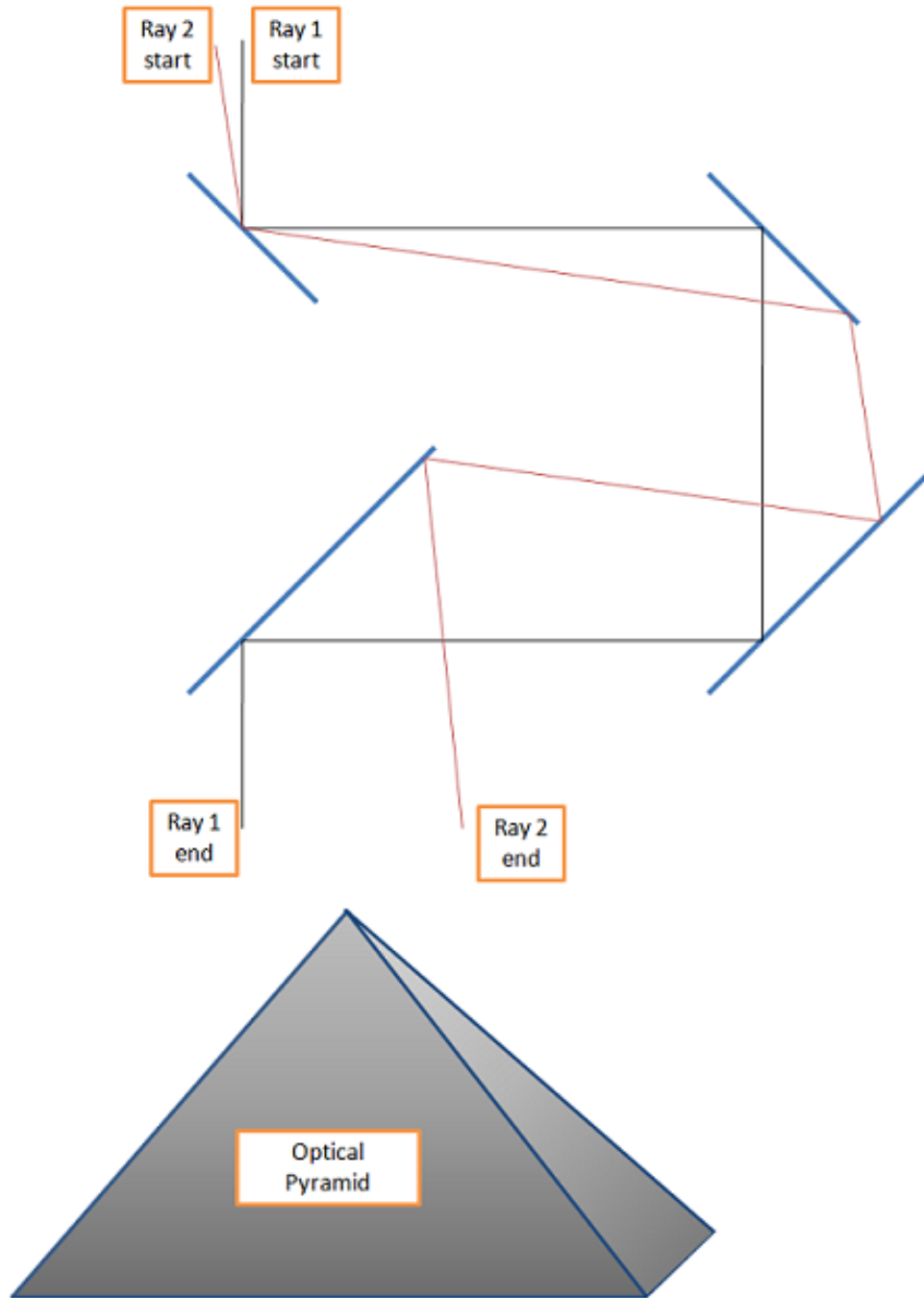
Figure 3.1: A LC SLM can change the angle of the light hitting the four mirror system. This figure shows two possible options for light coming off the diffractive optic. Ray 1 experiences no offset, whereas Ray 2 has an angular offset imparted by the LC SLM. This figure is not drawn to scale so that the effects of the four mirrors can be easily seen. The small initial angular offset of Ray 2 becomes a large offset after the series of reflections. This spatial displacement will make the light hit one of the four sides of the optical pyramid. Each side goes to a different beam path.
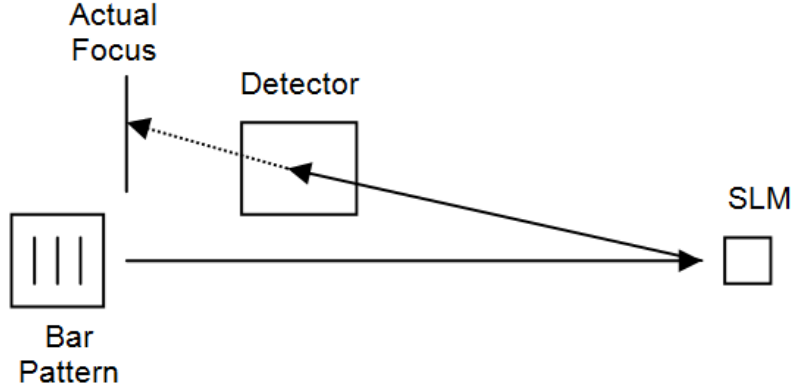
Figure 3.2:   A three-bar pattern is refelected off a LC SLM and has an ideal focus on the detector. However, if the the actual location of the focus is in a different plane, a large focus aberration can occur. Here the SLM is assumed to act as a both a reflective and focusing element.

$$\frac{1}{s_o} + \frac{1}{s_i} = \frac{1}{f_o} \tag{3.1}$$

As an example of creating focus error, consider the following setup. A three-bar pattern is refelected off a LC SLM. This pattern ideally would focus on a detector, but is actually focused at a point quite different (see Fig. 3.2).

If s_o is the distance from the LC SLM to the bar pattern, then s_i is the distance from the LC SLM to the actual image plane, and f is the focal length of the SLM. Assuming the detector is displaced, the actual image plane distance is from the LC SLM to the detector - henceforth known as z_a. As stated previously, if the ideal image plane (z_i) is different, then focus error will occur. The type of aberration incurred from z_i not equal to z_a was investigated further. To do this, it is necessesary to define the optical transfer function (OTF) for this system. As stated in Goodman [5], the OTF for a square aperture is given by

$$
\begin{aligned}
H(f_X, f_Y) = & \; TRI\left(\frac{f_X}{2f_o}\right) TRI\left(\frac{f_Y}{2f_o}\right) * \\
& SINC\left[\frac{8W_m}{\lambda}\left(\frac{f_X}{2f_o}\right)\left(1-(\frac{|f_X|}{2f_o})\right)\right] SINC\left[\frac{8W_m}{\lambda}\left(\frac{f_Y}{2f_o}\right)\left(1-(\frac{|f_Y|}{2f_o})\right)\right]
\end{aligned}
\tag{3.2}
$$

where an aperture of width $2w$ has a path length error (found by subtracting ideal phase distribution from the actual phase distribution) at the edge of the aperture of

$$
W_m = -\frac{1}{2}\left(\frac{1}{z_a} - \frac{1}{z_i}\right) w^2
\tag{3.3}
$$

The z_a and z_i described by Goodman are the same quantities described in this section. That means this OTF allows for determining the system behavior as the ideal and actual image planes differ.

3.2.2 Simulating Focus Aberrations.

Three-bar patterns were generated (see Fig. 3.3) in `Matlab`® using ones for the bars and zeros for everything else. The image was then scaled by 1000, 100, 50, 30, 10, and 5 photons per pixel respectively to create SNRs ranging from 2.2 to 31.6 (square root relationship for light coming from an incoherent source). This simulated a variable average number of incident photons. It is assumed that the pattern is resized to fit only a 128×128 pixel portion of a 256×256 LC SLM with pixel spacing of 15 microns and overal size of 7.68 mm $\times$ 7.68 mm. This was done to greatly reduce computational time needed to run multiple cases concurrently, all of which require multiple Fourier transforms and convolutions. Simulations were done at a wavelength of 1 micron. The width w described in Eq. (3.2) corresponds to half the size of the LC SLM.

Once the unblurred, scaled patterns were created, the next step involved incorporating differing locations of ideal and actual image planes. The ideal image distance
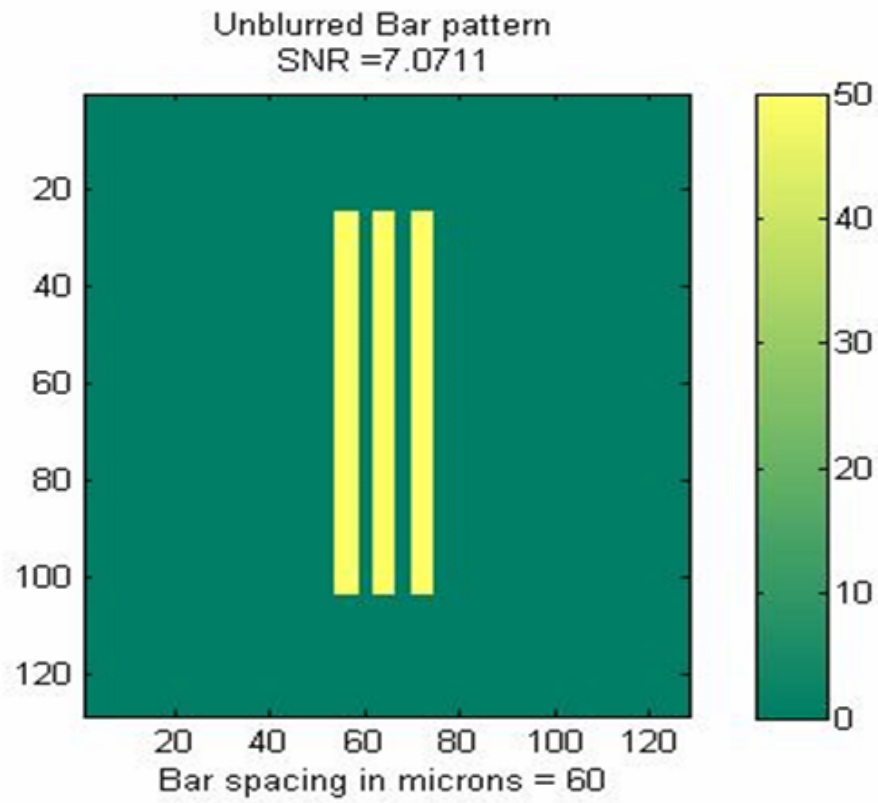
Figure 3.3:   An unblurred three-bar pattern scaled by SNR from the average number of incident photons.

Figure 3.4:   A blurred three-bar pattern scaled by SNR from the average number of incident photons per pixel. The ideal image plane is 1 m, while the actual image plane was at 3m. This leads to a three-bar pattern with focus aberration.

was set to 1 m. If the detector was placed here, the result would be a well-focused image. This, however, is a trivial result, so z_a was allowed vary. Values for z_a included 1.3m, 1.6m, 1.9m, 3m, 6m, and 10m. If this were setup on a real bench, then a camera would record a blurry bar patters that changed based on z_a. Simulating this requires not only the bar pattern, but the OTF for a square aperture, as seen in Eq. 3.2. The two-dimensional fast Fourier transform of the unblurred bar pattern was convolved with the OTF. The inverse two-dimensional fast Fourier transform of the convolution yields the blurry bar pattern. The extent of the blurriness depends upon how different z_a is from z_i. An example can be seen in Fig. 3.4.

3.2.3   Adding Noise.

Up to this point, the light incident on the three bar pattern has been missing a key component - noise. Assuming the light emerging from the field is generated by an incoherent source, then the noise should be Poisson in nature. [4] Adding Poisson
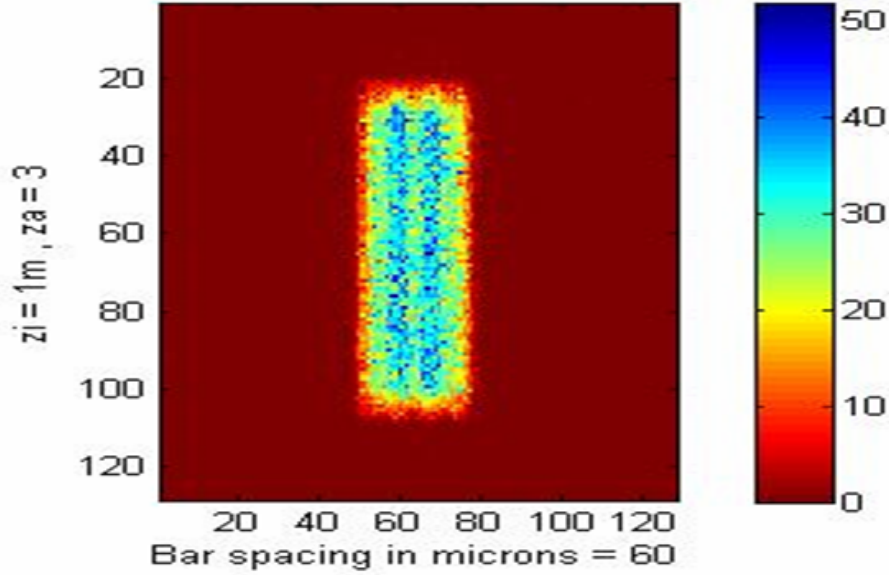
Figure 3.5: A blurred three-bar pattern scaled by SNR from the average number of incident photons. The ideal image plane is 1m, while the actual image plane was at 3m. This leads to a three-bar pattern with focus aberration. The addition of Poisson random noise further complicates the image.

random noise to an image is a simple process with the Matlab® "poissrand" command. The actual amount of noise seen by a real system varies greatly, and too many possible variables exists to model it in a way to determine how much noise should be added. Lacking this constraint, enough noise was added to see the effect on the simulated system. The effect of adding noise can be seen in Fig. 3.5.

3.2.4 Correcting Noisy Focus Aberration.

The ideal process for correcting the noisy, blurry pattern comes from the Richardson-Lucy algorithm. [21] The basic idea of the algorithm is that the most likely number of counts at a given pixel value in the latent image is calculated from the observed count from a pixel in the blurry image and the PSF that relates the two points. This process is done iteratively to retrieve the latent image. Conveniently, Matlab® contains an interative form of this type of deconvolution that is capable of taking into account additive noise. All that is needed is the noisy, blurry pattern and the PSF. The PSF

23
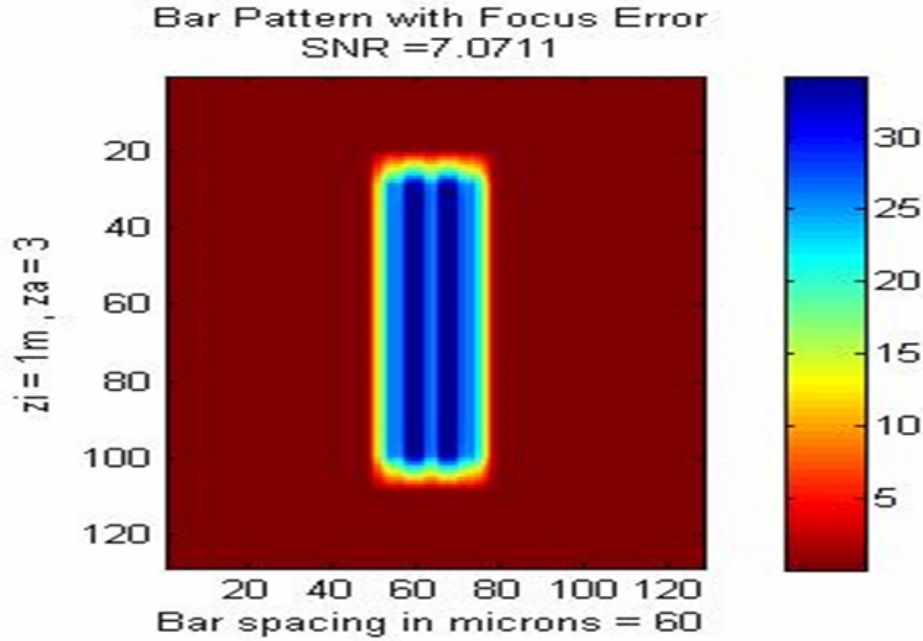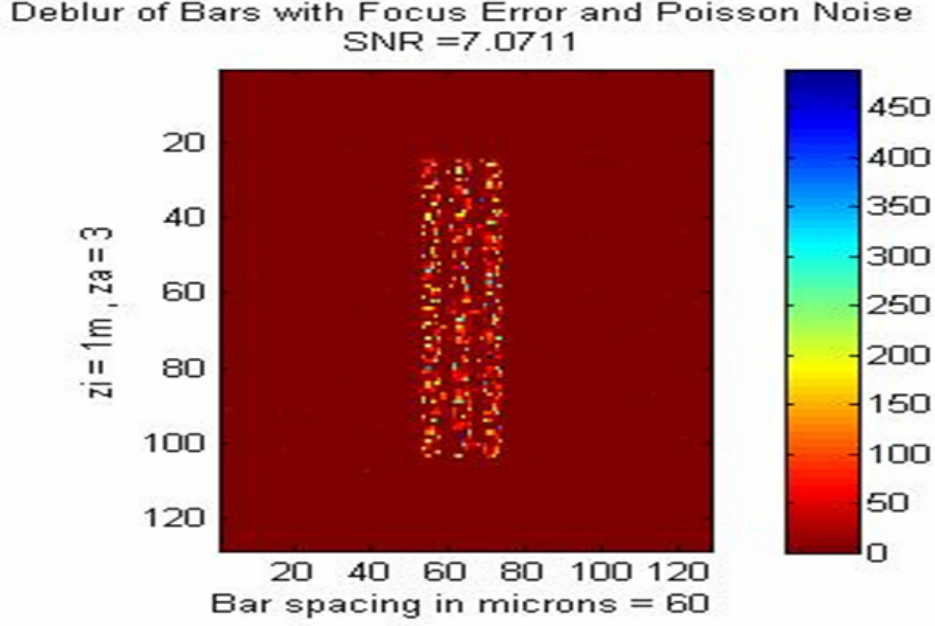
Figure 3.6:   A deblurred three-bar pattern scaled by SNR from the average number of incident photons. The ideal image plane is 1 m, while the actual image plane was at 3m. This leads to a three-bar pattern with focus aberration. The addition of Poisson random noise further complicates the image. Deconvolving the noisy image retrieves the orginal pattern, but is degraded due to the noise.

is easily obtained from the inverse two-dimensional fast fourier transform of the OTF. The algorithm includes a damping term that sets a threshold deviation between iterations for each pixel value. Pixels that go past the damping value are not included in future iterations, which is a way to help lower noise generation from running multiple iterations. The default number of 10 iterations was varied in increments up to 200. The latent image seemed to stabalize at 100 iterations, so this deconvolution was performed for each image. This can become a slow process if the size of the grid is large. Choosing only a 128×128 helped speed this along considerably. Without noise, a corrected pattern simply appears the same as the original image. However when noise is included, the retrieved pattern, while recognizeable, can be severaly degraded (Fig. 3.6).

24

The SNR of the incoming incoherent light plays a significant role in retrieving the original image. This is an important aspect to consider, because it could impose a SNR contraint that is more strict than a consraint based soley on camera requirements. As z_a increases, a higher and higher SNR is needed to reconstruct the original image. The quality of that reconstruction also depends highly on the SNR. When z_a is 1.9m, the three-bar pattern is barely discernable at a SNR of 2.2 (Fig. 3.7). At a z_a of 3m, it takes a SNR of 3.16 to even tell that the original image is three bars (Fig. 3.8). Increasing z_a out to 10m reveals a dramatic drop in detail at low SNR (Fig. 3.9). It takes a SNR of 5.47 before identifiable image recovery takes place. Of course different readers could pin these constraints at different values, based on individual perceptions. However, the point of the importance of SNR when considering how out of focus one can go while still reconstructing an image is quite clear. The code used for this process can be seen in Fig. 3.10.

3.3 Designing the Nonmechanial Zoom Telescope

Upon reaching this point, a method for the design had to be choosen. A variety of software packages exist that are fully capable of completing this task, but one in particular stood out - Code V. Worldwide, Code V is the most used optical design software. It has been used for many famous designs, including the corrective prescription for the Hubble Space Telescope. Computations and analysis done inside the program are remarkably fast due to the surface-to-surface geometrical ray tracing used for every situation.

3.3.1 Initial System Choices.

The first step in Code V is creating a new lens. An important note is that unless otherwise specified, all distances in the program are reported in milimeters. After starting a new lens, it is necessary to choose an entrance pupil diameter. A size of 250mm was choosen for this research in order to keep the complete design small. Although the SLM would limit the operating bandpass, three different wavelenghts

Figure 3.7:   A three-bar pattern with focus aberration from $z_i = 1$m and $z_a = 1.9$m is shown for various SNRs. As SNR decreases, the original three bar pattern is more difficult to discern. This is due to the amount of Poisson random noise added to the original image.

Figure 3.8: A three-bar pattern with focus aberration from $z_i = 1$m and $z_a = 3$m is shown for various SNRs. As SNR decreases, the original three bar pattern is more difficult to discern. This is due to the amount of Poisson random noise added to the original image.
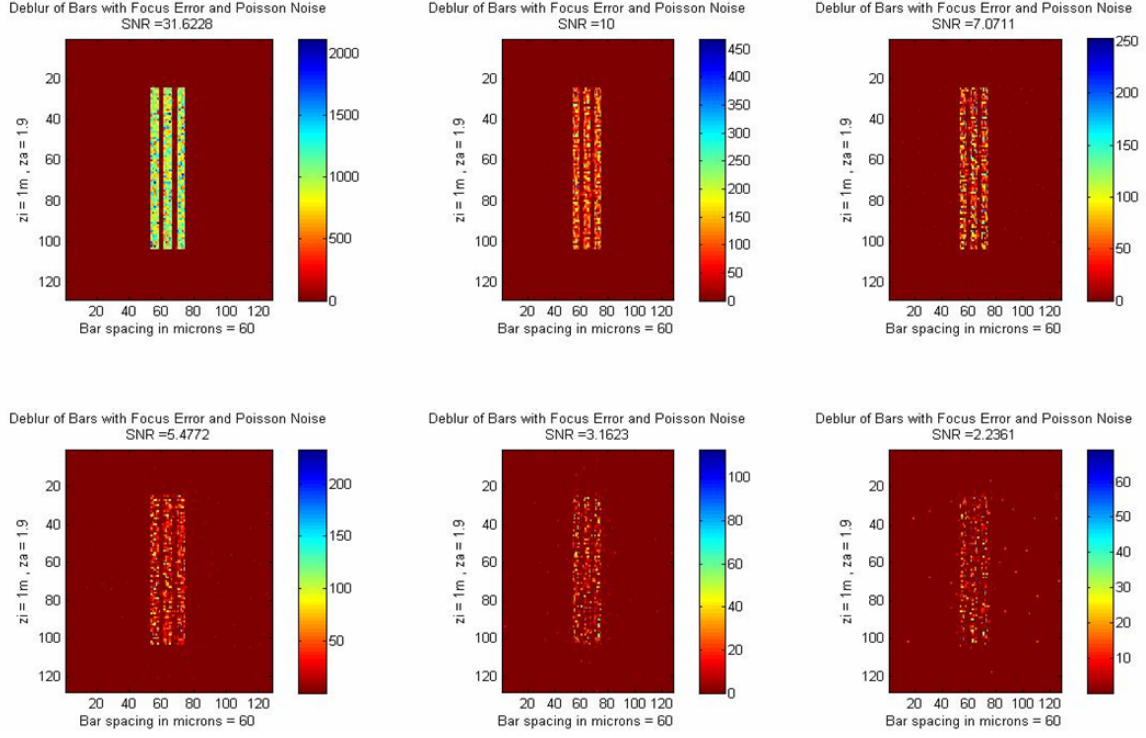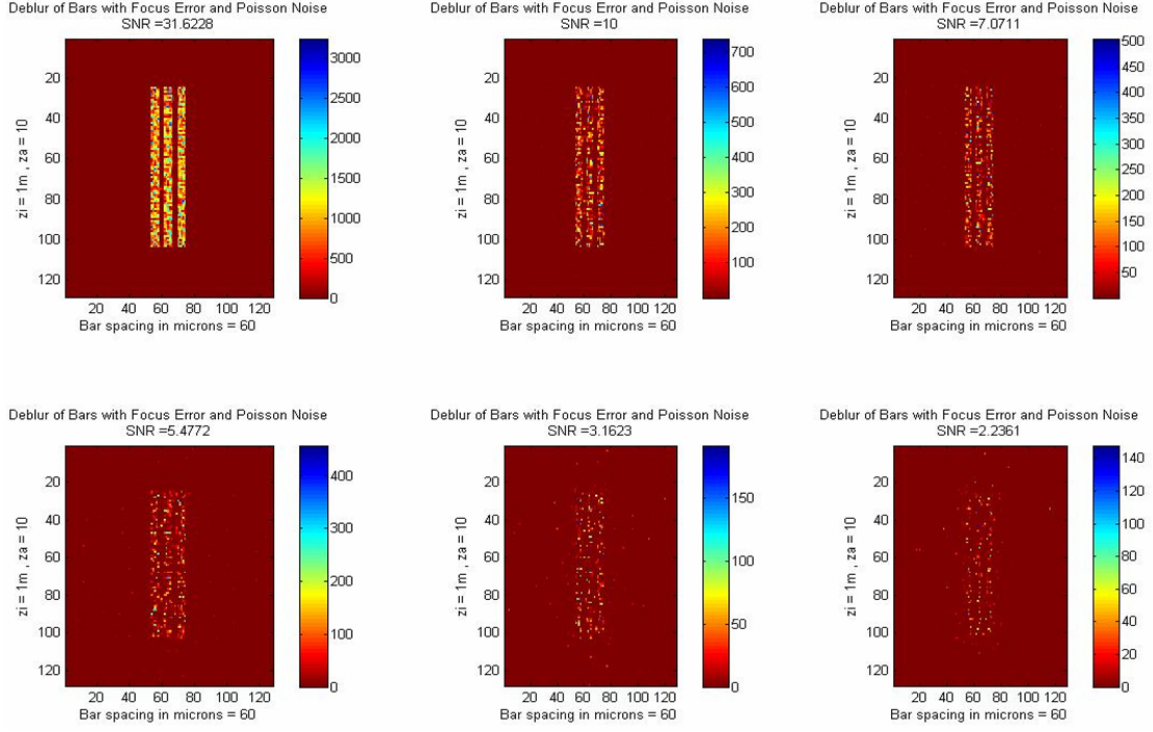
Figure 3.9: A three-bar pattern with focus aberration from $z_i = 1$m and $z_a = 10$m is shown for various SNRs. As SNR decreases, the original three bar pattern is more difficult to discern. This is due to the amount of Poisson random noise added to the original image.
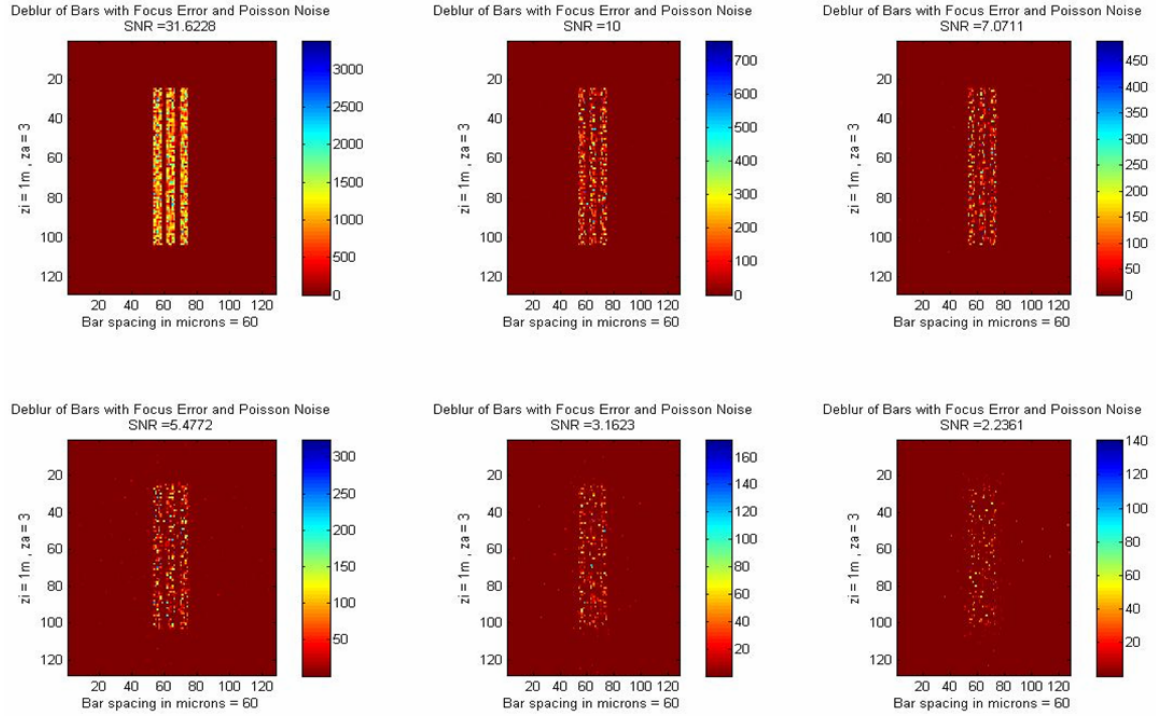
```
while kk<=nn
    Wm = -.5*((1/za(kk)) - (1/zi))*w^2;   %Max path length error
    NumWavesDefocus = Wm/lam ;             %number of waves of defocus
    AnumWaves = d^2/(16*lam*zi*sqrt(3));
    fo = (d/2)/(lam*za(kk));   %Cutoff wavelength
    fx = x/(lam*za(kk));
    fy = y/(lam*za(kk));

    fprintf(' %8.4f %20.4f %20.4f \n',zi,za(kk),NumWavesDefocus)

    Hfxfy = tri(fx/(2*fo)).*tri(fy/(2*fo)).*sinc(((8*wm)/lam)*(fx/(2*fo)).*(1-(abs(fx)/(2*fo)))).*...
    sinc(((8*wm)/lam)*(fy/(2*fo)).*(1-(abs(fy)/(2*fo))));

    [m n] = size(Ibar);
    ii=1;
    while ii<=n

        barpattern = bz*Ibar(ii);
        figure(kk)
        subplot(2,3,ii)
        imagesc(barpattern)
        title(['Unblurred Bar pattern' cr 'SNR =' num2str(SNR(ii))])
        xlabel(['Bar spacing in microns = ' num2str(barspace*delta1*1e6)])
        %ylabel(['zi = 1m , za = ' num2str(za(kk))])
        colormap(summer);
        colorbar

        blurrybars=ifftshift(real(ifft2(fftshift(Hfxfy.*ifftshift(fft2(fftshift(barpattern)))))));
        figure(6+kk)
        subplot(2,3,ii)
        imagesc(blurrybars)
        title(['Bar Pattern with Focus Error' cr 'SNR=' num2str(SNR(ii))])
        xlabel(['Bar spacing in microns = ' num2str(barspace*delta1*1e6)])
        ylabel(['zi = 1m , za = ' num2str(za(kk))])
        colormap(flipud(cmap));
        %xlim([150 350]);
        %ylim([150 350]);
        %colormap(cmap);
        colorbar

        blurwithnoise = poissrnd(abs(blurrybars));
        figure(12+kk)
        subplot(2,3,ii)
        imagesc(blurwithnoise)
        title(['Bar Pattern with Focus Error and Poisson Noise' cr 'SNR =' num2str(SNR(ii))])
        xlabel(['Bar spacing in microns = ' num2str(barspace*delta1*1e6)])
        ylabel(['zi = 1m , za = ' num2str(za(kk))])
        colormap(flipud(cmap));
        %xlim([150 350]);
        %ylim([150 350]);
        %colormap(cmap);
        colorbar

        deblurfocus =deconvlucy(blurwithnoise,ifftshift(real(ifft2(fftshift(Hfxfy)))),100,1);
        figure(18+kk)
        subplot(2,3,ii)
        imagesc(deblurfocus)
        title(['Deblur of Bars with Focus Error and Poisson Noise' cr 'SNR =' num2str(SNR(ii))])
        xlabel(['Bar spacing in microns = ' num2str(barspace*delta1*1e6)])
        ylabel(['zi = 1m , za = ' num2str(za(kk))])
        colormap(flipud(cmap));
        %xlim([150 350]);
        %ylim([150 350]);
        %colormap(cmap);
        colorbar
        ii = ii+1;

    end
    kk=kk+1;
end
```

Figure 3.10:   This code blurs the original three-bar pattern using the OTF, adds Poisson random noise, and deconvolves the focus error for a variety of SNR values.
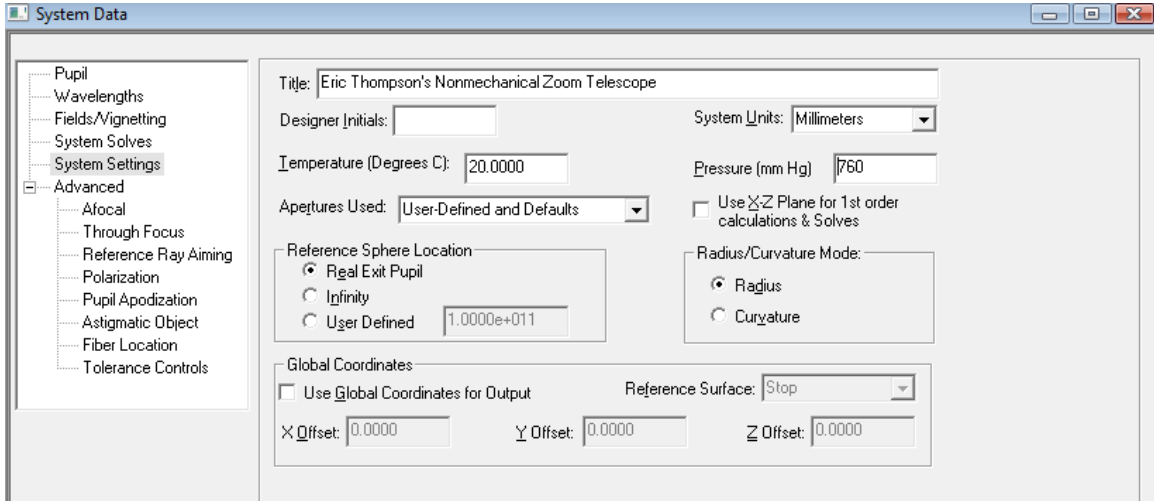
Figure 3.11: Standard operation conditions, using the standard visible wavelegths (d,c,f spectrum), were chosen for the initial setup. All results were found using these settings. If this design were to built for an application, it is extremely important these variables are changed to the appropriate values for the setup.

are traced through the system: 656nm, 587nm, and 486nm. This was done soley to investigate any chromatic issues with the choosen lenses. This is important because the LC SLM may have a limited bandpass, but the region it operates in can vary. Field angles of up to 60 arcseconds were also introduced. All results were computed at a temperature of 20 degrees Celsius and an atmospheric pressure of 760mm Hg - both of which are standard values (see Fig. 3.11).

3.3.2 Creating Surfaces.

Once the initial conditions are set, it is time to start building the system. Code V does everything based on surfaces through the Lens Data Manager. The object, stop, image plane, as well as every component are designed as a series of surfaces (see Fig. 3.12). Surfaces can be added one at a time or as a group. Once added, each surface type must be chosen. As seen in Fig. 3.12, a wide variety of options are available. Even after choosing the type of surface, hundreds of options are available for customization to fit a specific system. Some of the important options include further definition of the shape (for example, radius of curvature), cements or coatings, and size (see Fig. 3.13). It is even possible to import interferograms, which enables

Surface #	Surface Name	Surface Type	Y Radius	Thickness	Glass	Refract Mode	Y Semi-Aperture	X Semi-Aperture	Non-Centered Data
Object		Sphere	Infinity	1.0000e+007		Refract			
Stop		Conic	-742.8572 V	-260.0000		Reflect	75.0000	75.0000	
2		Conic	-290.2328 V	300.0000 V		Reflect	22.5000	22.5000	
3		Sphere	Infinity	-81.9076 S		Reflect	13.8884	13.8884	Decenter & Bend
4		Sphere	-20.3422	-6.0000	743972.4	Refract	4.7510	4.7510	
5		Sphere	-30.0000	-4.4438		Refract	4.0191	4.0191	
6		Sphere	47.3533	-1.2500	755201.2	Refract	3.5217	3.5217	
7		Sphere	-19.5727	-4.8646		Refract	3.4588	3.4588	
8		Sphere	-50.0000	-4.2742	743972.4	Refract	3.7909	3.7909	
9		Sphere	220.0000	-150.0000		Refract	3.8231	3.8231	
10		Sphere	Infinity	70.0000		Reflect	10.0000	7.6800	Decenter & Bend
11		Sphere	Infinity	-50.0000		Reflect	10.0000	7.6800	Decenter & Bend
12		Sphere	Infinity	30.0000		Reflect	10.0000	7.6800	Decenter & Bend
13		Sphere	Infinity	-50.0000		Reflect	10.0000	7.6800	Decenter & Bend
14		Sphere	Infinity	190.0000		Reflect	10.0000	7.6800	Decenter & Bend
15		Sphere	-207.2875			Reflect	7.6800	7.6800	Decenter & Bend
16		Sphere	Infinity	10.0000 S		Refract	10.0000	10.0000	
Image		Sphere	Infinity	-0.0167 V		Refract	12.5000	12.5000	

End Of Data

Dropdown options: Sphere, Cylinder, Conic, Asphere, X Toroid, Y Toroid, Thermal Gradient, Spline, Anamorphic Asphere, Lens Module, User Defined

EFL: -14918.6838 | f/ 59.6747 | DIM: Millimeters | Apertures Used: User-Defined and Defaults | Use ZX Plane: No | Polarization Ray Tracing Active: No

Figure 3.12: When adding a surface to the Lens Data Manager, it is necessary to specify the type of surface that is being encountered. This can range from a simple spherical surface, a complex asphere, a customized set of Zernike polynomials, or a wide variety of other options.

accurate modeling of lens surfaces measured in the laboratory. Zernike polynomials can be used to create a surface that models any type of aberration. Due to modeling complexity, though, the LC SLM will be treated as a flat surface for the presented analysis.

After a surface is completely defined, it is necessary to express the distance to the next surface as well as the index of refraction encountered on the way to that surface. All major glass catalogs are included if it is necessary to find a specific glass. Custom indices may also be entered. Finally, the size of the surface (aperture) and whether light is reflecting or refracting off of it must be specified. If defining a lens, the specified thickness should be the center width of the lens.

3.3.3 Designing the System.

Designing the nonmechanical zoom telescope requires all of the components

Figure 3.13: After a surface type is choosen, it is necessary to fully define its properties in the current system. While many options are availbe, some important things to include are the types of coatings and any transparencies for the wavelengths used.

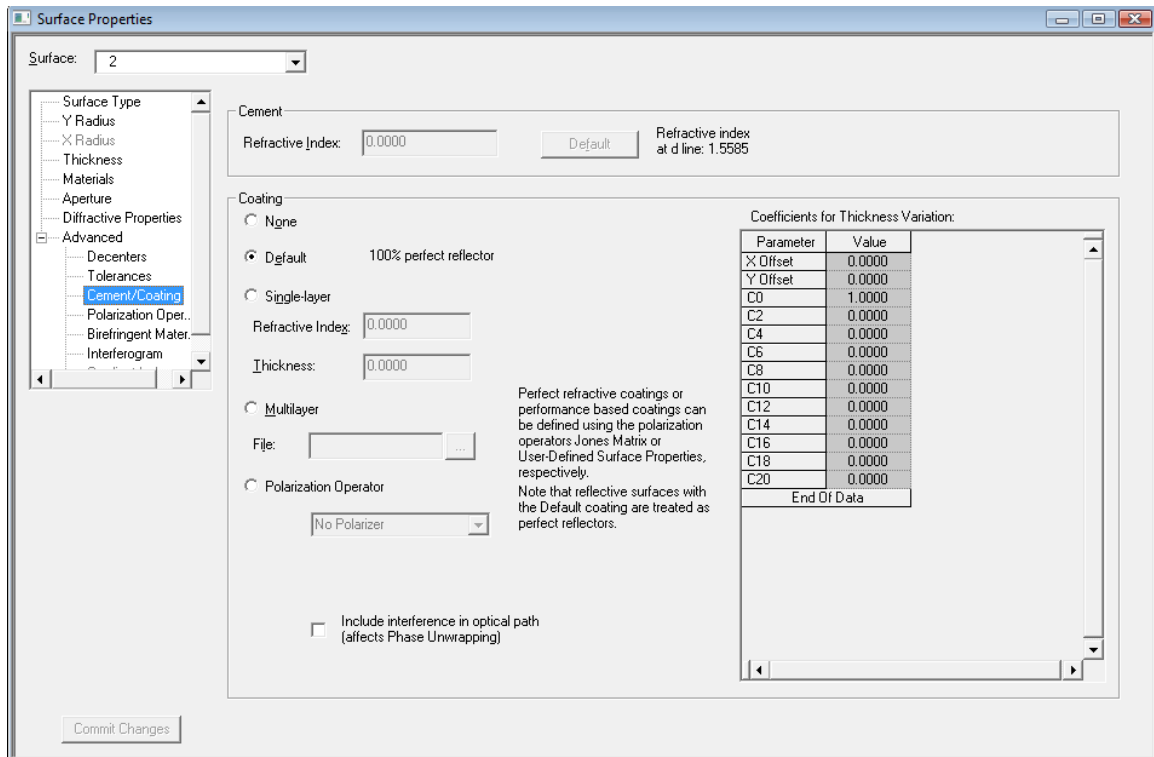previously discussed as well as a host of analytical tools offered in Code V. The first step is deciding how much light to capture. Keeping the goal of a compact system in mind, the primary mirror (first surface) is only six inches in diameter (150mm). The secondary mirror (45mm) reflects light from the primary on to an angled flat mirror placed before the cassegrain focus (Fig. 3.14). Both the primary and secondary are conics and only use a y radius of curvature and conic constant for definition. This combination creates a f/# for the system. A slower system, larger f/#, means that less of a curvature is needed in the first two mirrors. Reducing curvature means a reduction in other types of aberrations, such as spherical. An added bonus is that keeping these two components simple makes them inexpensive to purchase.

When the light hitting the angled flat mirror after the secondary is deflected, it continues to come to a focus. However, in order to use the LC SLM in a fashion similar to previous research, the light must be collimated or nearly collimated. Besides needing collimation, the size of the beam must be matched to the LC SLM. To incorporate both needs while keeping aberrations low, a Cooke triplet was introduced (Fig. 3.14). Spreading out the work over six surfaces is what minimizes extra aberrations. Every surface in the triplet is spherical with either a positive or negative radius of curvature. Avoiding any complex conic or asphric surfaces keeps cost of components low.

Code V makes it quite easy to ensure that light emerging from the triplet is collimated or nearly collimated. Instead of calculating everything by hand, a "solve" can be added to the radius or thickness of a surface. Adding a solve will change the numerical value of that particular part. For example, the radius of curvature of the sixth surface on the triplet can be determined automatically with a solve so the angle of the exiting y marginal ray is zero degrees. This guarantees collimated light approaching the LC SLM. This can be checked by making sure marginal ray height remains constant on subsequent flat surfaces. For this system, the light is nearly collimated hitting the LC SLM, and slowly comes to a focus in the image plane.
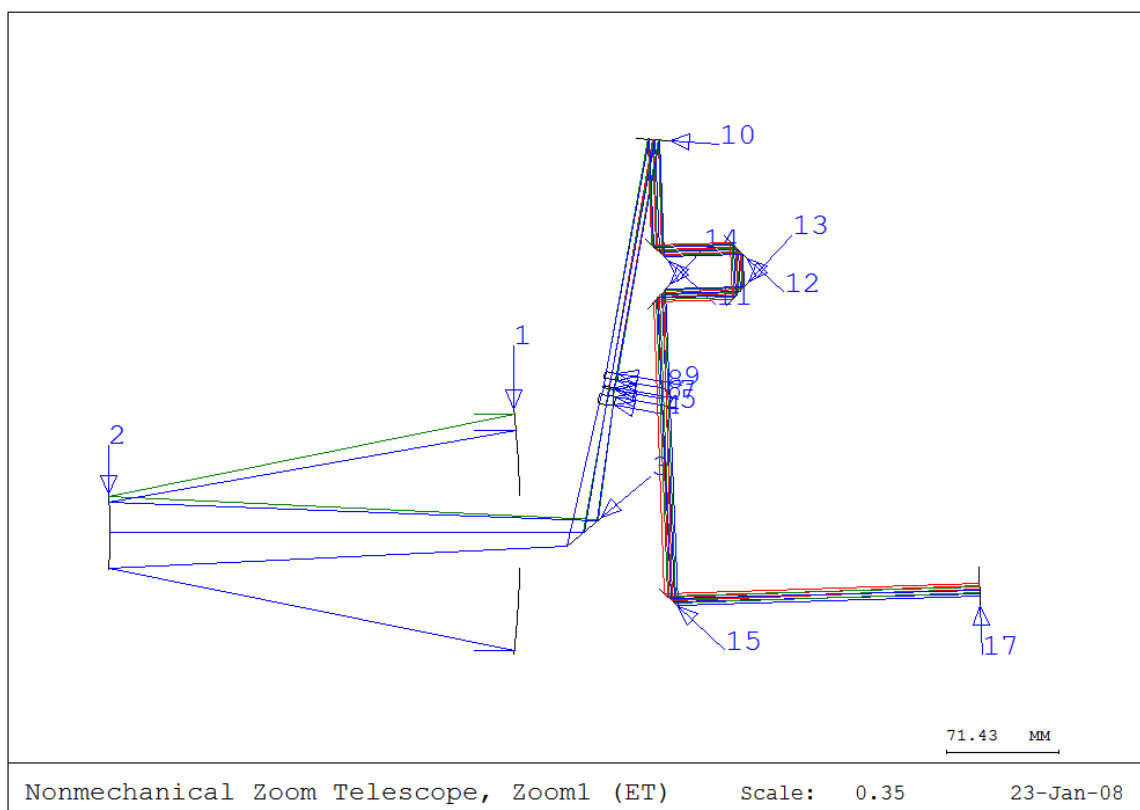
Figure 3.14:   This is a two-dimensional drawing of the in-focus beam path for the nonmechanical design. Surface 10 represents the LC SLM and surface 15 represents one side of the optical pyramid. The image plane is located at surface 17. The Cooke triplet (surfaces 4-9) imparts just enough focus so that the focal plane coincides with the image plane.

The LC SLM and the next four mirrors are for angle selection and angle magnification (surfaces 10-14 in Fig. 3.14). This concept was discussed and proven in section 3.1. Depending on the angle across the LC SLM, light will hit one of four sides of the optical pyramid. One of those sides is represented by surface 15. This particular zoom has the focal plane coinciding with the image plane.

Four different paths exist, but only two of them are easily visible in two dimensions. The second of these can be seen in Fig. 3.15. Light from the LC SLM comes from a slightly different angle, and so surface 15 reperesents a different side of the optical pyramid. Light in this path is directed to a curved mirror. The mirror, purposefully, does not focus the light in the image plane. Doing this creates a larger, out-of-focus image on the camera. As seen earlier in this chapter, the focus aberration can be removed, and this will leave a larger, in-focus picture after post-processing.

The next two surfaces are not easily seen using two-dimensional visualization. This is because the remaing two sides of the optical pyramid would send the light either into or out of the page. As before, a slight angle across the LC SLM is magnified by the next four mirrors. This holds true for going into and out of the page as well. Fortunately, Code V allows for surfaces to be tilted freely in a three-dimensional environment. Figures 3.16 and 3.17 show the remaining two zooms. The concept is identical to that of Fig. 3.15, except the curvature across surface 17 is increased by different amounts. Increasing the curvature makes the light focus further and further in front of the image plane, thus creating larger and larger focus errors. The larger the focus error, the further the chief ray height is from the optic axis in the image plane. Post-processing can correct for this to reveal larger and larger images corresponding to higher zooms.

3.4 Methodology Summary

The concept of angle and selection and magnifiaction with four mirrors and a LC SLM allow for selecting multiple different beam paths nonmechanically. To have optical zooms, the focus along each path must be different, and may not coincide with
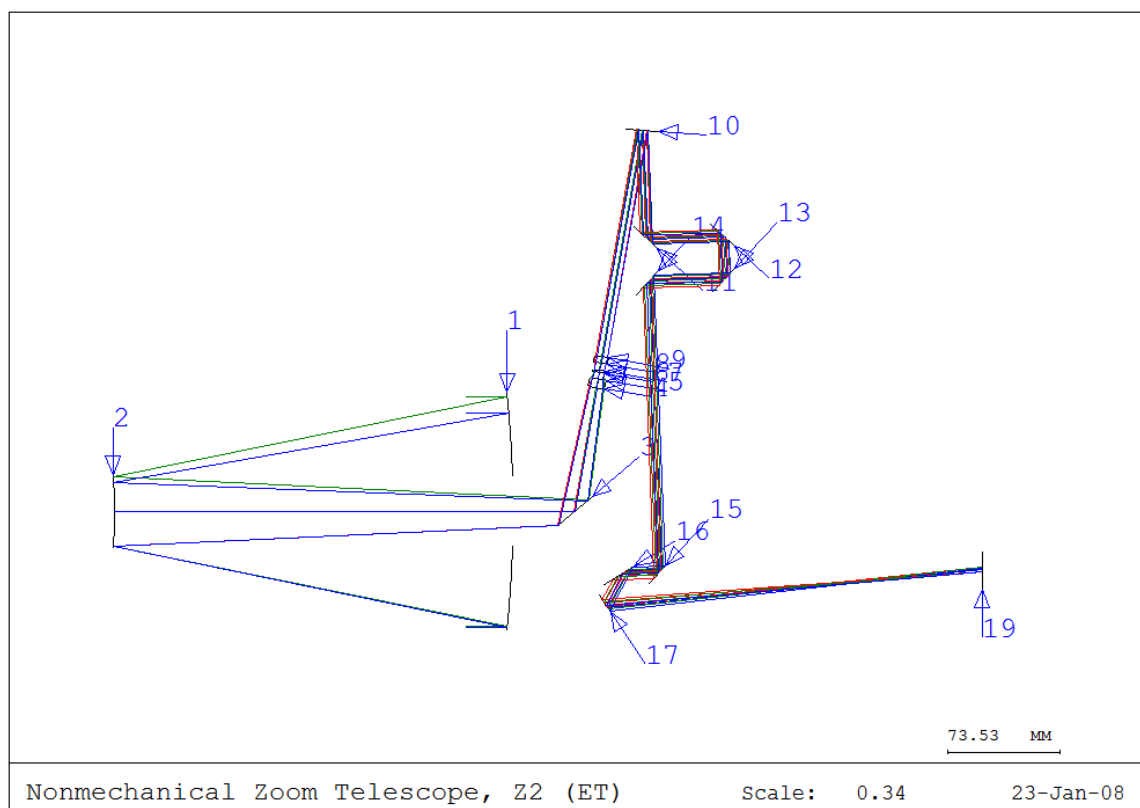
Figure 3.15: This is a two-dimensional drawing of an out-of-focus beam path for the nonmechanical design. Surface 10 represents the LC SLM and surface 15 represents one side of the optical pyramid. The image plane is located at surface 19. Curvature on surface 17, however, causes the focal plane to be in front of the image plane. This generates a larger, but out-of-focus image on the camera that can be corrected with post-processing
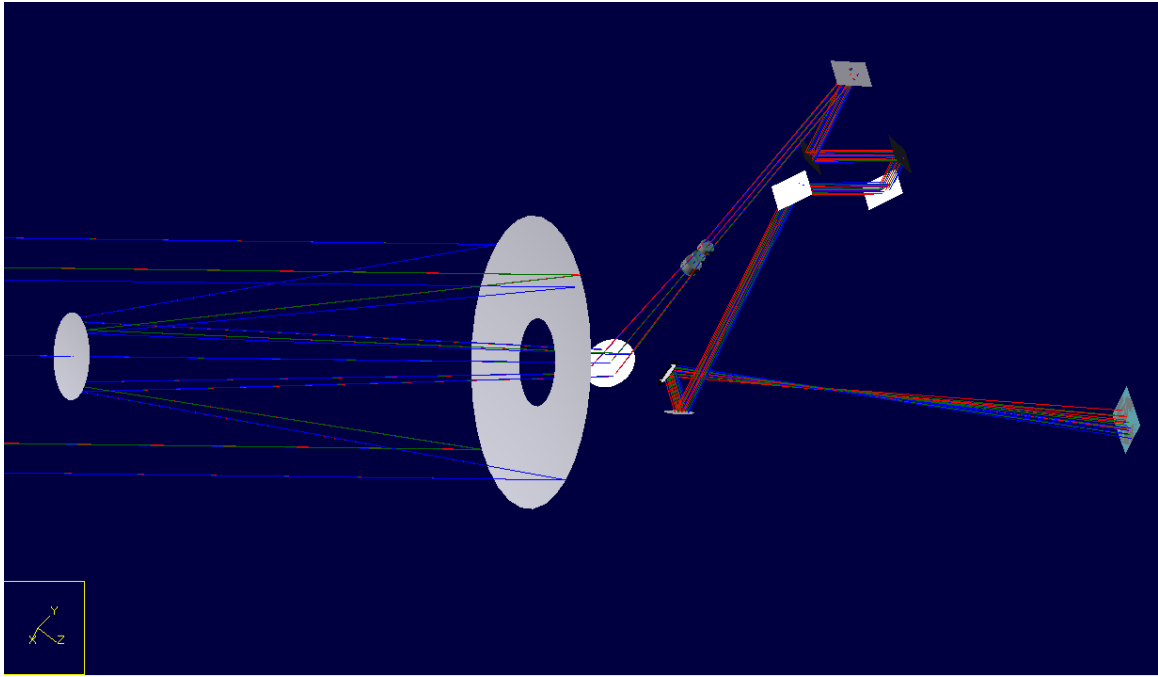
Figure 3.16: This is a three-dimensional drawing of an out-of-focus beam path for the nonmechanical design. The lens layout is nearly identical to Figure 3.15, but represents a different path. Curvature along this path is greater, causing the focal plane to be further in front of the image plane. This generates a larger, but out-of-focus image on the camera that can be corrected with post-processing
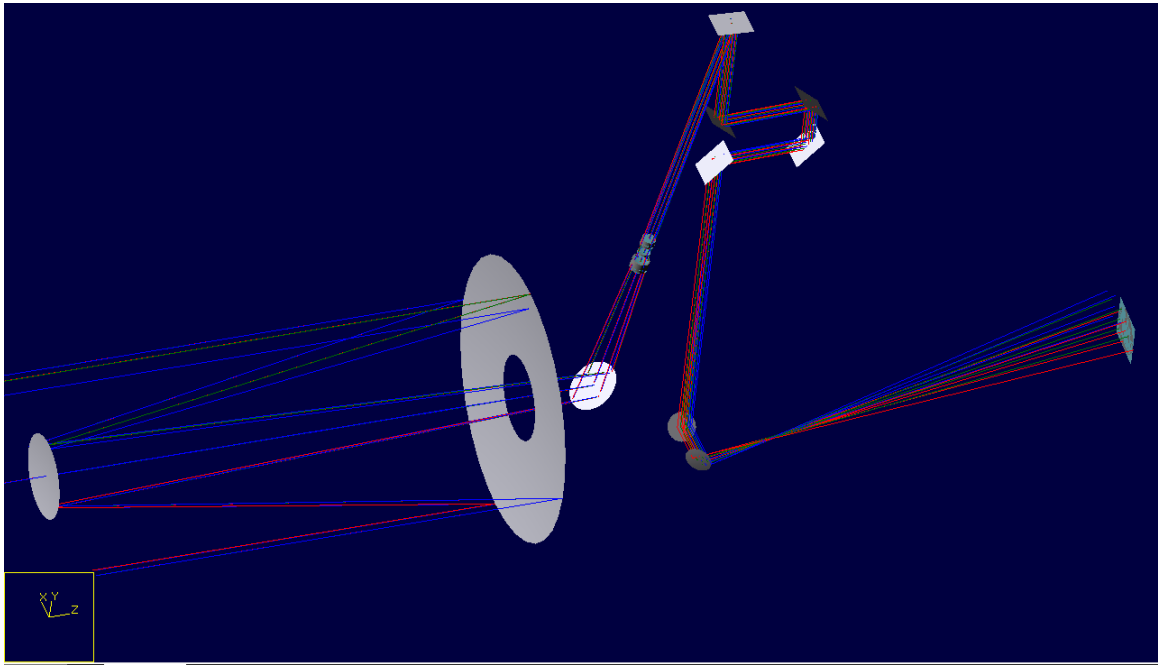
Figure 3.17:   This is a three-dimensional drawing of an out-of-focus beam path for the nonmechanical design. The lens layout is nearly identical to Figure 3.16, but represents a different path. Curvature along this path is greater, causing the focal plane to be even further in front of the image plane. This generates an even larger, but out-of-focus image on the camera that can be corrected with post-processing

the image plane. Even though this creates focus error, it can be corrected with post processing. The diffractive nature of the LC SLM also adds a 40 wave focus subrange to each path. This can all be accomplished using inexpensive, simply shaped optical components. Code V proved to be an incredibly flexible and in-depth design tool that was well-matched for this research. The two and three-dimensional viewing tools were extremely helpful for visualizing all aspects of the design.

IV. Results and Analysis

This chapter presents system performance analysis of the nonmechanical multi-zoom telescope. The method of focus correction through post-processing shows that optical zooms of up to 3× are easily achieveable. Many diagnostic tests such as spot diagrams, third order wavefront analysis, and point spread functions are included. A detailed look into optimization shows that wavefront aberrations can be reduced in the system. The magnitude of aberrations revealed that a single LC SLM could correct for imperfections in the system - thus eliminating the need for any complicated and expensive surfaces. A different approach using a standard magnification process shows that post processing can be eliminated if system complexity is increased. This type of design can easily reach optical zooms of up to 10×. However, both methods are scaleable, meaning the 3× and 10× zooms shown here are not the limits of design for each system.

4.1 Aberrations Before the LC SLM

Before reaching the angle selection process, the beam is already aberrated. This is due to contributions from the primary mirror, secondary mirror, and the Cooke triplet. The two telescope mirrors establish an initial focus. The curvature of these two mirrors plays an important role. Ideally, the system will be slow (large f/#). This can be done with small curvature across the primary and secondary. Also, smaller curvature across each mirror results in smaller spherical aberration in the system. However, as curvature decreases, the size of the secondary must increase in order to reflect light from the edges of the primary - it is not reflecting toward the optical center as closely. Another option for keeping the secondary small is to move it far away from the primary, but this detracts from creatign a compact system. Increasing the size of the secondary increases the amount of light blocked over the size of the aperture, which lowers the signal received by the system. Obviously a balance of received light versus aberrations caused must be reached.

One option for keeping the amount of light blocked minimized is to use more complicated surfaces for the mirrors. Such surfaces could keep the secondary small relative to the primary while keeping a large f/#. This however, greatly increases cost. Another option is to use a smaller f/# and just resize the beam while changing the focus. A singlet can change the focus if the beam is the right size. A doublet could resize the beam, if necessary, and change the focus. Resizing may be necessary in order to make the beam fill the LC SLM. The presented system is based on a 7.68mm square LC SLM, but is easily changed to account for a different size. An added benefit of making the beam smaller is that the cost of all subsequent optics in the system is reduced.

It is important that resizing and changing the focus only adds a minimal amount of aberration to the beam. However, depending on the magnitude of change needed in focus and size, the curvature of a singlet or doublet can significanly add to spherical aberration. A solution for this quandry is a Cooke triplet, which resizes the beam and changes the original focus. Using six surfaces instead of two or four allows the necessary curvature to be spread out among several lenses. Making only this change reduced spherical aberration, the dominant aberration by an order of magnitude, contribution by 26 percent. Knowing the optimal amount of curvature to place across each of the six surfaces is difficult. One option is to iteratively change each surface in small amounts and examine the third order aberrations. This extremely tedious process was tried, but reduced aberrations by no more than 5 to 10 percent. Fortunately, Code V provides its own internal optimization process. To do this, the curvature of each lens in the triplet is changed to a variable quantity. The software can then be directed to search for a solution with minimized third-order spherical aberration (see Fig. 4.1). This is a convenient feature, but a large number of constraints must be entered before the process is started to ensure the result uses components that are still easy to manufacture. An example of this is constraining the glass to regions of the glass catalog that are inexpensive. The end result was an additional 20 percent
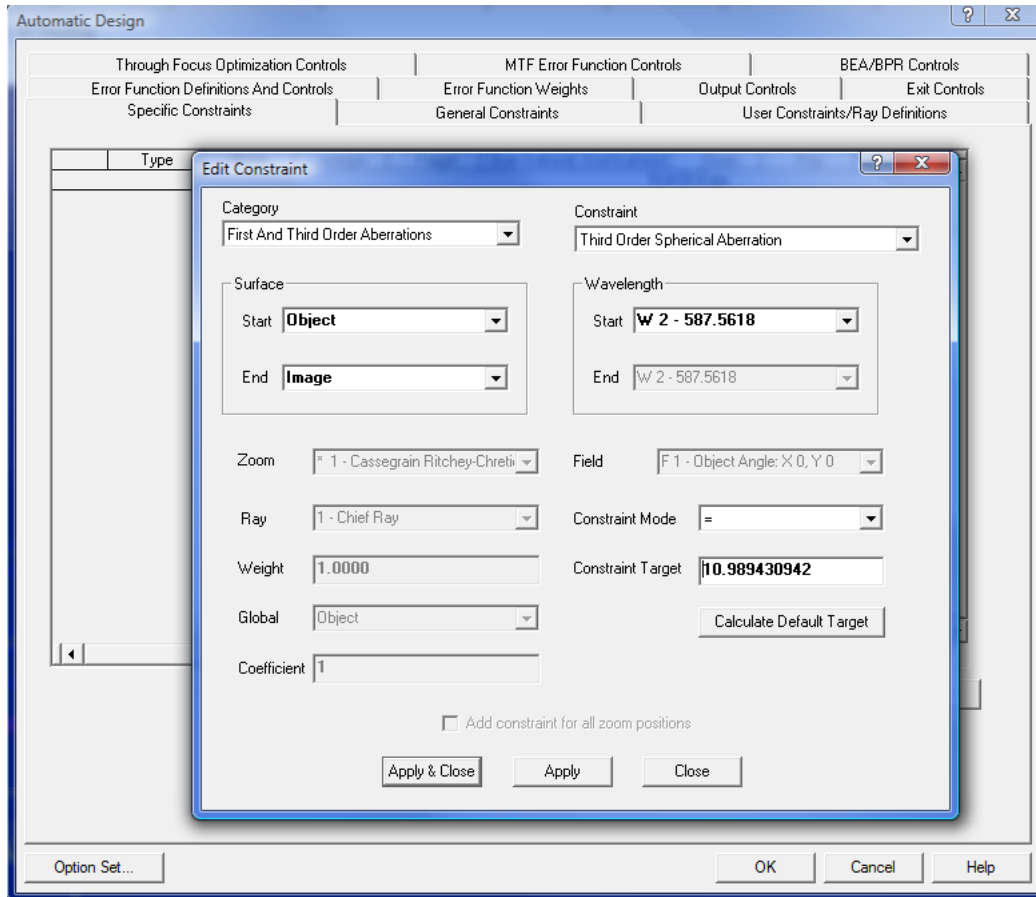
Figure 4.1: Third-order spherical is the largest aberration introduced by the primary, secondary, and Cooke triplet. This is due to constraining these surfaces to be made using simple conic and spherical shapes, which keeps cost low. Reducing this aberration is important because the LC SLM has limited corrective ability. Code V provides an iterative process for reducing aberrations. This run reduced spherical aberration of the beam going to the LC SLM by 20 percent.

reduction in spherical aberration in the beam going to the LC SLM. This is beneficial because the LC SLM has limited corrective ability.

4.2 Analysis of System Requiring Post-processing

This section shows the results of the system design that requires a post-processing focus correction. The advantage of this system over a normal magnification process, which will be shown later, is that it needs significantly fewer optical components. This makes alignment much easier and greatly reduces weight of the overall design.

It also reduces cost. One drawback, obviously, is the need for post-processing. The other drawback is that to achieve larger zooms, more light can be lost if rays close to the marginal diverge from the optic axis such that they are not captured by the detector. A zoom of $3\times$ is easily achievable with minimal light loss. This is dependant on detector size and can easily be increased.

Each optical path presents its own unique set of aberrations and magnifications. This is due to the various curvatures in the mirrors directing the light towards the image plane. By changing the curvatures, the height of the chief ray on the image plane increases or decreases. A larger chief ray yields a larger image. As seen in Chapter 3, even when a large focus error exists, post processing can retrieve the original image if SNR is high enough.

4.2.1   Height of Chief Ray.

Code V uses geometric ray tracing to determine many properties of the system, including height of the chief and marginal rays. A paraxial ray trace through zoom 1 of the design (see Fig. 3.14) confirms that the light is indeed focused on the image plane. This can be seen by looking at the height of the marginal rays (see Fig. 4.2). Tracing through zoom 4 (see Fig. 3.17) shows that the height of the chief ray is nearly $3\times$ larger in magnitude. The marginal rays, however, are not focused. As discussed previously, this can be corrected with post-processing. This is just an example and is not meant to show a maximum achievable zoom using this process. The amount of zoom achievable is also dependent on the particular type of object being imaged, SNR, and detector size to give an exhaustive list of possibilities.

4.2.2   Defocus.

Repeatedly in this research, it has been said that a large focus aberration is pivotal. There is a contraint on the focus though that must be made clear. In order for the post-processing to work easily, the focus must be nearly constant across the image - regardless of the magnitude. Another way of saying this, is that there should not be a large focus-dependence based on field angle. This is clearly obvious in

	HMY	UMY	N * IMY	HCY
EP	125.000000	0.000013		0.000000
STO	125.000000	0.336526	-0.168257	0.000000
2	37.503257	-0.078090	-0.207308	0.075782
3	14.076184	0.078090	-0.078090	0.319888
4	7.680000	0.205834	0.299449	0.386535
5	6.444994	0.199139	0.015694	0.340699
6	5.560065	0.062936	-0.316556	0.319040
7	5.481394	-0.101030	0.381084	0.319192
8	5.972864	-0.006971	0.220488	0.380145
9	6.002660	0.008142	-0.035426	0.396991
10	4.781428	-0.008142	-0.008142	1.226664
11	4.211520	0.008142	-0.008142	1.613845
12	3.804443	-0.008142	-0.008142	1.890403
13	3.560196	0.008142	-0.008142	2.056337
14	3.153119	-0.008142	-0.008142	2.332895
15	1.606225	0.008142	-0.008142	3.383814
16	-0.081415	0.008142	-0.008142	4.530352
IMG	-0.000136	0.008142		4.475133

(a) Zoom 1

	HMY	UMY	N * IMY	HCY
EP	125.000000	0.000013		0.000000
STO	125.000000	0.336526	-0.168257	0.000000
2	37.503257	-0.078090	-0.207308	0.075782
3	14.076184	0.078090	-0.078090	0.319888
4	7.680000	0.205834	0.299449	0.386535
5	6.444994	0.199139	0.015694	0.340699
6	5.560065	0.062936	-0.316556	0.319040
7	5.481394	-0.101030	0.381084	0.319192
8	5.972864	-0.006971	0.220488	0.380145
9	6.002660	0.008142	-0.035426	0.396991
10	4.781428	-0.008142	-0.008142	1.226664
11	4.211520	0.008142	-0.008142	1.613845
12	3.804443	-0.008142	-0.008142	1.890403
13	3.560196	0.008142	-0.008142	2.056337
14	3.153119	-0.008142	-0.008142	2.332895
15	1.606225	0.008142	-0.008142	3.383814
16	1.402687	-0.036195	-0.022168	3.522092
17	-7.548218	-0.036195	-0.036195	-12.529985
IMG	-7.547612	-0.036195		-12.528900

(b) Zoom4

Figure 4.2: This figure shows two different zooms for the telescope. Here"HMY" stands for height of the marginal ray and "HCY" is the height of the chief ray. The height is tracked as it progresses past each surface, finally ending on the detector. Plot (a) shows the in-focus zoom. Plot (b) shows an out-of-focus zoom with a larger image on the detector. Post-processing out the defocus would yield a nearly $3\times$ larger image than plot (a).

(a) Zoom 1   (b) Zoom4
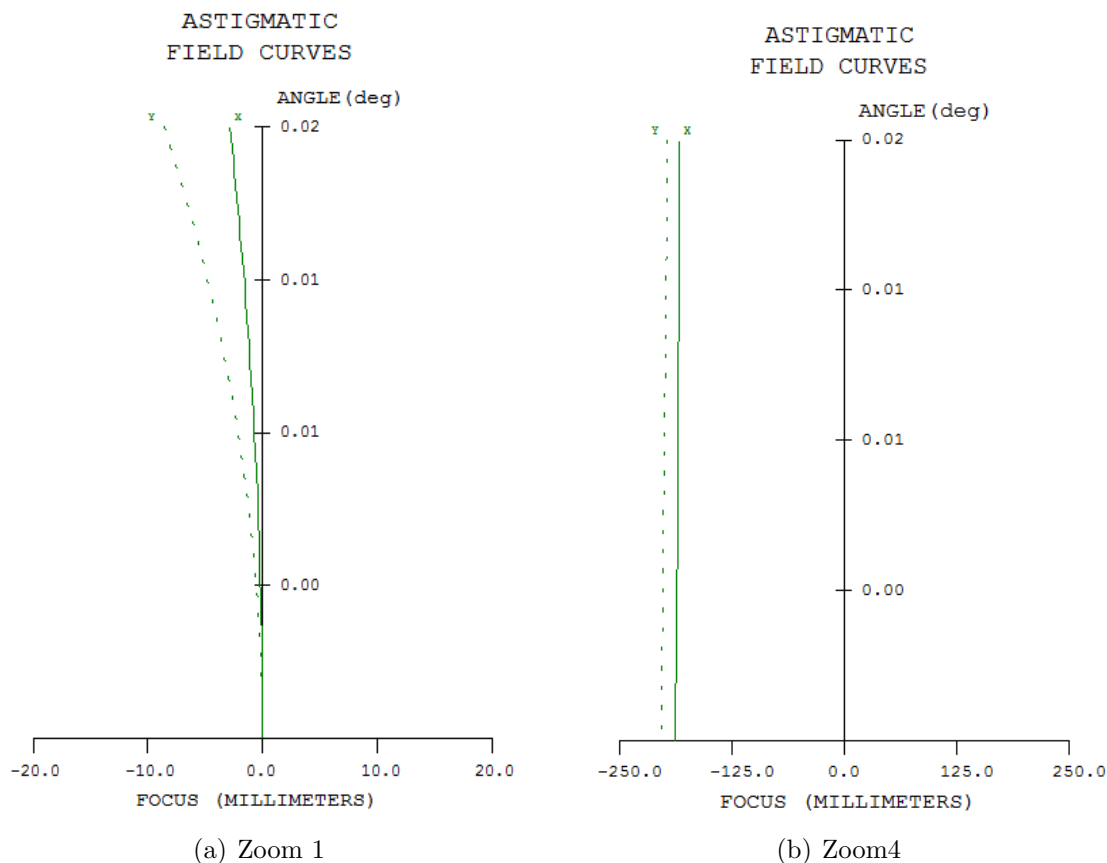
Figure 4.3:   This figure shows two different zooms for the telescope. Plot (a) shows that the focus aberration as a function of field angle for the in-focus zoom is small. Plot (b) shows the out-of-focus zoom that yields a $3\times$ larger image on the detector. The focus error is large, but fairly constant across the field. Astigmatism over the field has not been removed completely, but this shows that it is possible to pick a best-focus to use for post processing.

Fig. 4.3. Not all of the astigmatism has been worked out of this system, but picking a best-focus for correction is easily possible. As field of view increases, so does focus error. This is acceptable for small fields of view, but could be hard to correct for wide field-of-view systems.

4.2.3   Spot Diagrams.

An analysis of the spot diagrams shows that this system is not diffraction limited. The in-focus zoom has a tight spot for the on-axis light (see Fig. 4.4), but as field angle increases, the spot gets more spread out. Most of the light falls within a

(a) Zoom 1

(b) Zoom4

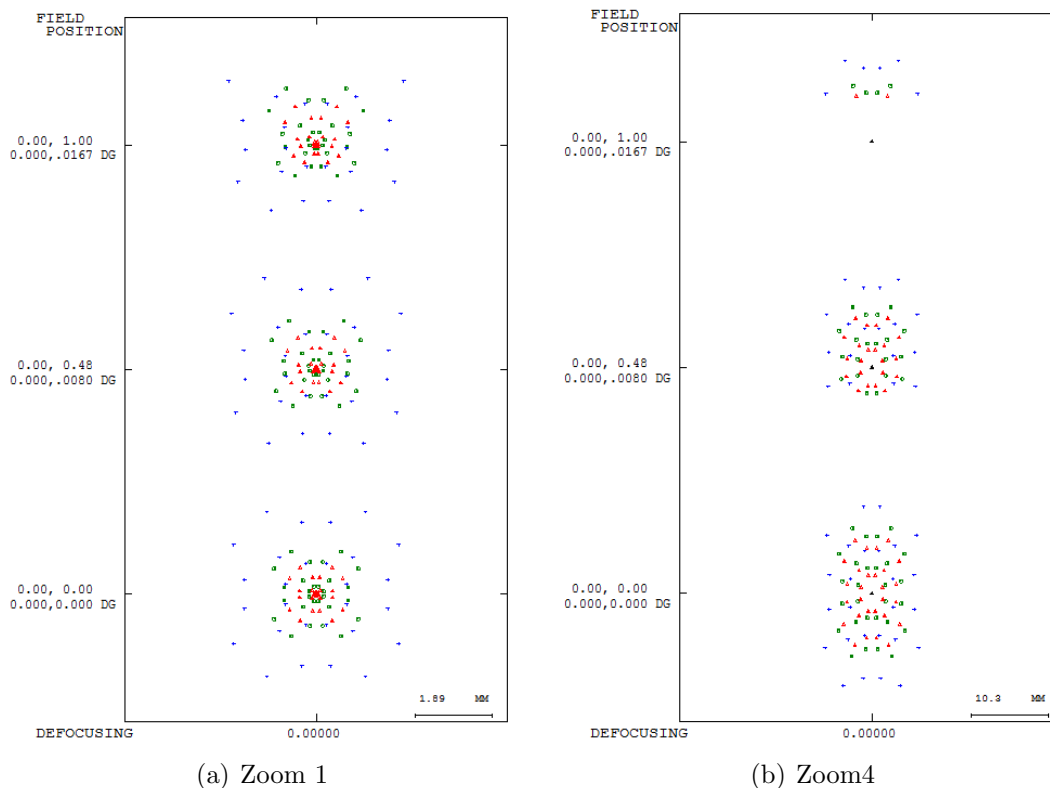Figure 4.4: This shows spot diagrams for two different zooms of the telescope. The colors represent wavelengths of the d, c, f spectrum, and the three spots are shown at different field angles. Plot (a) shows that the in-focus zoom is not producing a diffraction-limited spot. Further optimization could reduce this size and should be done if trying to build this system. Plot (b) shows the spot diagram for the out-of-focus zoom that yields a $3\times$ larger image on the detector. As expected, the extreme focus error causes the spot to be spread out greatly. Chromatic aberration as a function of field angle dependence only appears lower in plot (b) due to the defocus.

1.9mm diameter circle. This would not yield a good image, but optimization could be done to decrease this size. The $3\times$ zoom has a very large spot diagram, with most of the light falling within a diameter of 10.3mm. This, however, is expected due to the extremely large aberrations before post-processing. Field angle dependence was not nearly as prevalent in the severely out-of-focus spot.

4.2.4   Point Spread Function.

An analysis of the point spread functions shows agreement with the findings from the spot diagrams. Ideally, the spot for the in-focus $1\times$ path would be smaller and

46

closer to the diffraction limit. However, an optimization of the optics and correction from the LC SLM could reduce the size greatly. The PSF showed little dependence on field angle for the in-focus path (see Fig. 4.5). The size of the beam in the image plane is very large for the 3× zoom path. It is so large, that even a 8192×8192 grid size is not accurately retrieving the PSF. Another approach outside of Code V should be used if this PSF is desired.

4.2.5   Third-Order Aberrations.

Third-order aberrations break down the different deviations seen in the beam. As expected, spherical aberration plays a large role. This is due to using simple surfaces. The next most-prevalent aberration is astigmatism for the in-focus paths and defocus for the paths needing correction. Both spherical and astigmatism could be reduced with optic optimization and LC SLM correction. A quick and simple analysis to do is called a ray aberration plot. These plots (see Fig. 4.6) confirm previous results and show spherical aberration, focus error, and astigmatism. The 3× out-of-focus image shows even larger aberration and astigmatism.

4.3   Analysis of System Not Requiring Post-processing

This section presents the results of the system design that does not require a post-processing focus correction. The advantage of this system, obviously, is that no post-processing is required to view captured data. This means no large focus aberrations are introduced into the system. Optical zooms of 10× are easily achievable with light loss controlled purely by reflective and diffractive efficiencies. The designs represented here show a 2×, 3×, and 10× optical zoom. The drawback is that many more optical components are needed. This increases cost, weight, and alignment complexity.

Magnification of a beam via a two-lens refractive system has been used since refractive telescopes came into existance. This simple, yet effective, method uses two
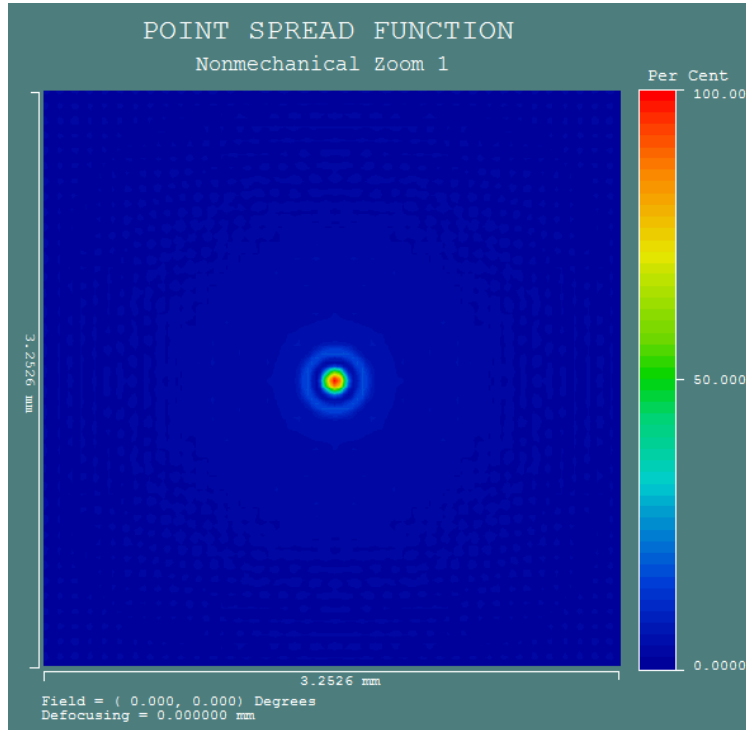
(a) Field Angle 0.0 deg
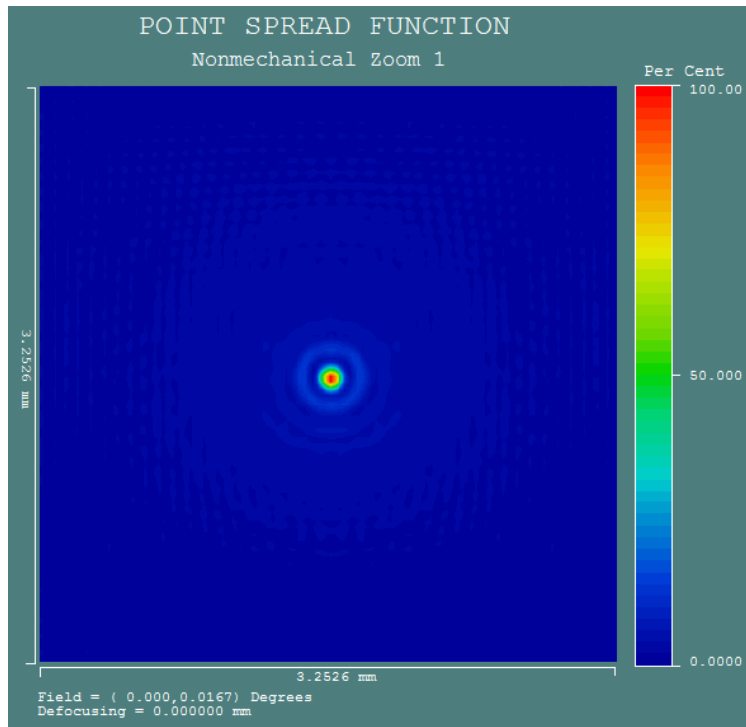
(b) Field Angle 0.02 deg

Figure 4.5:   This figure illustrates PSFs for two different field angles for the in-focus path of the telescope. Plot (a) shows the PSF for the on-axis light and plot (b) shows the PSF for the field coming at0.02 degrees field angle.
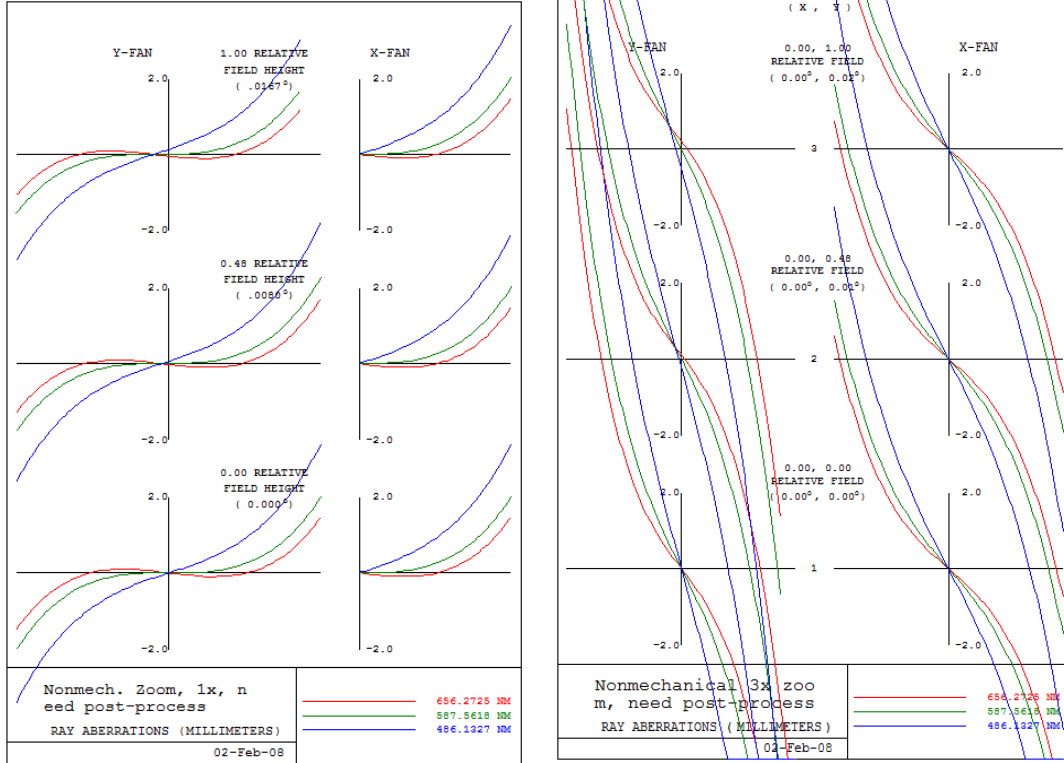
(a) Ray Aberration Zoom 1

(b) Ray Aberration Zoom 4

Figure 4.6:   This figure shows ray aberration curves for two different zooms of the telescope. Ideally the curves would be flat. Curving up and down at the sides indicates sperical aberation. Tilting across the origin indicates defocus. Diffrent focus tilts in the x and y fans indicate astigmatism. Plot (a) shows the curves for the in-focus zoom. Chromatic aberration is present in the different defocus slopes for each wavelength. Sperical aberration is present in all cases. Plot (b) shows the the curves for the $3\times$ out-of-focus image. Large spherical aberration and defocus are prevalent at every wavelenghth and field angle. Astigmatism is also easily seen.

Figure 4.7: Two-lens refractive systems have been used to change magnification since the first telescopes. The distance between the two lenses is set to be equal to the sum of their focal lengths. The ratio of the focal lengths determines the magnification power. If f_o is 2 times longer than f_e, then a magnification of 2 is achieved when the light is refocused in the image plane

lenses of different focal lengths. [6] The lenses are placed a distance apart equal to the sum of their focal lengths (see Fig. 4.7). Magnification power is determined by the ratio o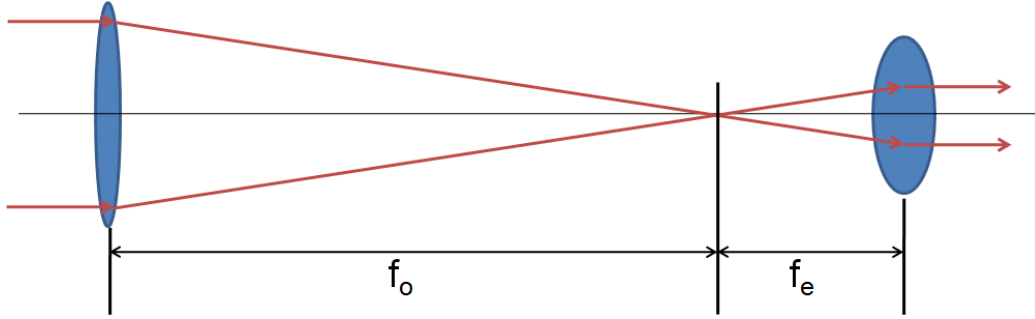f the focal lengths. If the first lens has a focal length two times longer than the second, then a magnification of 2 is achieved when light is focused in the image plane.

The key to making four different optical zooms nonmechanically with this method lies in the four different beam paths. A different set of optics for each path, having different focal length ratios, is all that is needed. A second optical pyramid allows the light from each path to be pointed back towards a single detector (see Fig. 4.8). By changing focal ratios, the height of the chief ray on the image plane increases or decreases. A larger chief ray yields a larger image. This method allows for specific zooms to easily be designed based on requirements for a given project.

Several differences in design of the optical path exist between this method and the previously described process. Instead of slowing the focus from the telescope, the Cooke triplet collimates the beam before it hits the LC SLM (see Fig. 4.8). The angle selection process does not change, light is still directed to one of four sides of an optical pyramid. Light emerges from each path collimated and is redirected towards the image plane with a second optical pyramid. This is represented by surface 15 in Fig. 4.8. At this point, light from each path is collimated. Another lens focuses the

Refractive Magnifiation, 1x   Scale: 0.35   03-Feb-08
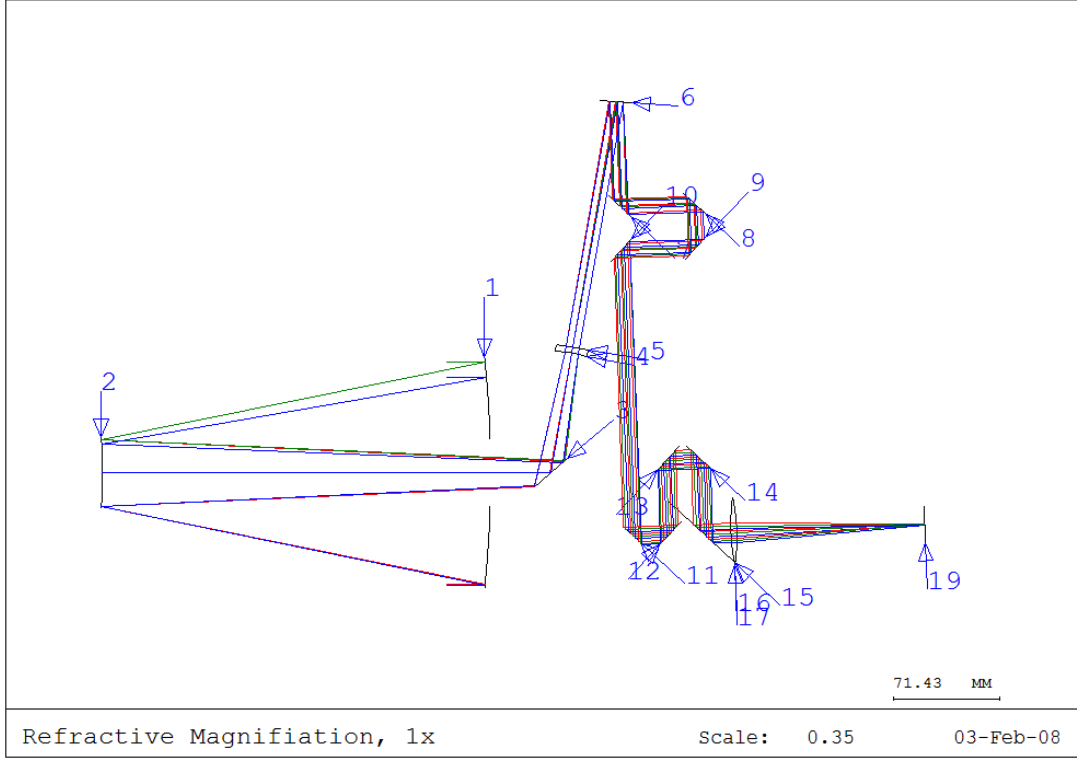
Figure 4.8:   Stardard refractive magnification can be used to resize the beam in
the image plane. This method requires more optics, but relieves the need for post-
processing. Surface 15 represents a second optical pyramid. This will allow light from
the four different paths to be directed to the SLM with minimal aberration.

light from each path onto the image plane. Figure 4.9 shows the path for a 2× zoom,
and Fig. 4.10 shows the path for a 10× optical zoom. The new beam path designs,
although more complicated, greatly reduce aberrations in the image plane.

4.3.1   Height of Chief Ray.

Code V uses geometric ray tracing to determine many properties of the system,
including heights of the chief and marginal rays. A paraxial ray trace through Fig. 4.8
confirms that the light is indeed focused on the image plane. This can be seen by
looking at the heights of the marginal rays (see Fig. 4.11). Tracing through Fig. 4.10
shows that the height of the chief ray is nearly 10× larger in magnitude. Unlike the
previous design, the marginal rays are focused - so no post-processing is needed. This
is just an example and is not meant to show a maximum achievable zoom using this

51

Figure 4.9:   Light from the first optical pyramid sends light down a beam path.
The distance between the two lenses along this path is set to be equal to the sum of
their focal lengths. The ratio of the focal lengths in this path is 2, thus leading to a
$2\times$ larger image on the camera. Light entering the final lens before the image plane
is collimated. The last lens focuses light onto the image plane.

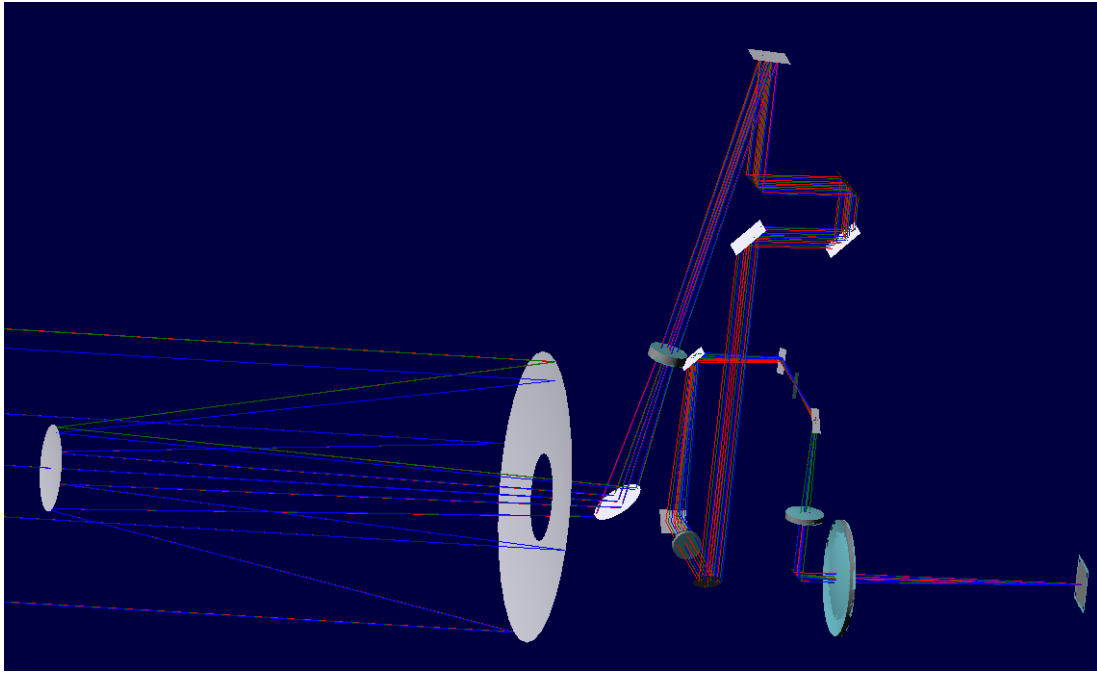Figure 4.10: Light from the first optical pyramid sends light down a beam path. The distance between the two lenses along this path is set to be equal to the sum of their focal lengths. The ratio of the focal lengths in this path is 10, thus leading to a 10× larger image on the camera. Light entering the final lens before the image plane is collimated. The last lens focuses light onto the image plane.
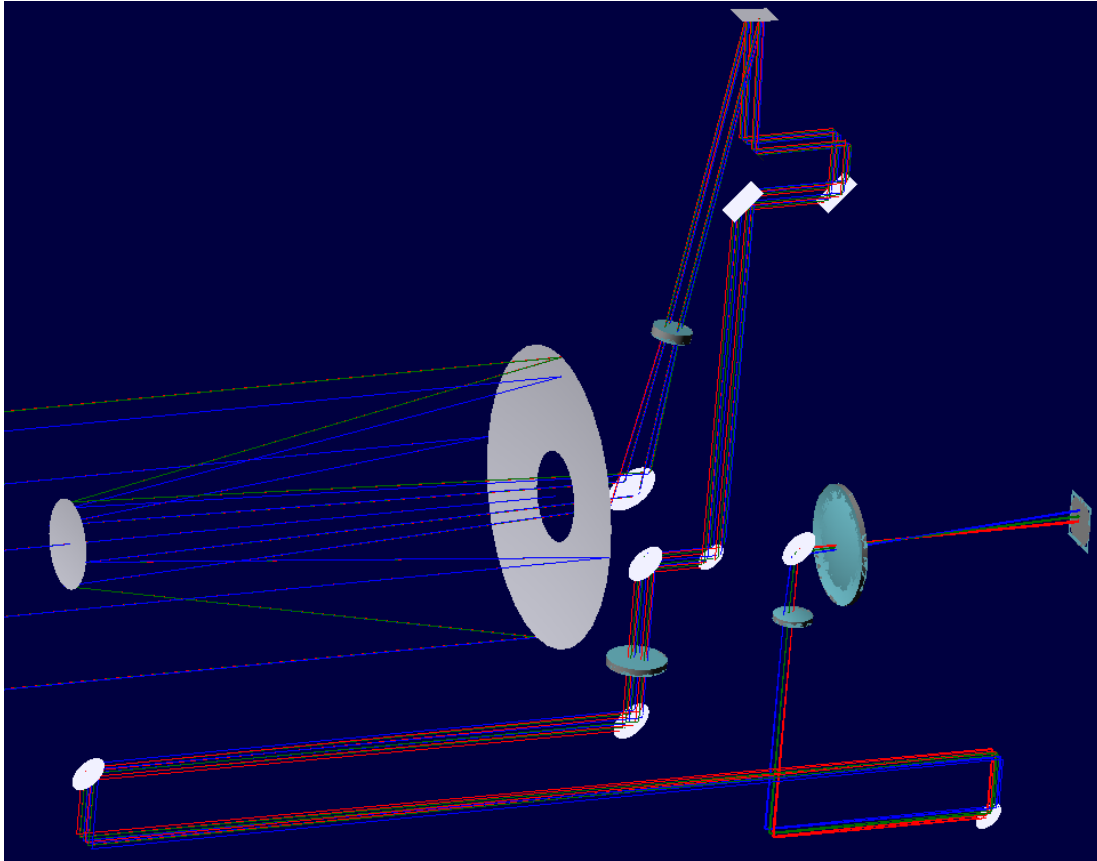
53

	HMY	UMY	N * IMY	HCY
EP	125.000000	0.000013		0.000000
STO	125.000000	0.336526	-0.168257	0.000000
2	37.503257	-0.078090	-0.207308	0.075782
3	14.076184	0.078090	-0.078090	0.319888
4	7.680000	0.000000	-0.229194	0.386535
5	7.680000	0.000000	0.000000	0.399046
6	7.680000	0.000000	0.000000	1.190496
7	7.680000	0.000000	0.000000	1.522574
8	7.680000	0.000000	0.000000	1.759773
9	7.680000	0.000000	0.000000	1.902093
10	7.680000	0.000000	0.000000	2.139291
11	7.680000	0.000000	0.000000	3.040647
12	7.680000	0.000000	0.000000	3.168735
13	7.680000	0.000000	0.000000	3.405934
14	7.680000	0.000000	0.000000	3.500813
15	7.680000	0.000000	0.000000	3.738012
16	7.680000	0.019987	0.058662	3.832892
17	7.600052	0.060317	-0.118368	3.805502
18	0.000081	0.060317	-0.060317	0.604070
IMG	0.000000	0.060317		0.604036

(a) Refractive Zoom 1×

	HMY	UMY	N * IMY	HCY
EP	125.000000	0.000013		0.000000
STO	125.000000	0.336526	-0.168257	0.000000
2	37.503257	-0.078090	-0.207308	0.075782
3	14.076184	0.078090	-0.078090	0.319888
4	7.680000	0.000000	-0.229194	0.386535
5	7.680000	0.000000	0.000000	0.399046
6	7.680000	0.000000	0.000000	1.190496
7	7.680000	0.000000	0.000000	1.522574
8	7.680000	0.000000	0.000000	1.759773
9	7.680000	0.000000	0.000000	1.902093
10	7.680000	0.000000	0.000000	2.139291
11	7.680000	0.000000	0.000000	3.040647
12	7.680000	0.000000	0.000000	3.206686
13	7.680000	-0.002510	0.007366	3.443885
14	7.669961	-0.007609	-0.014965	3.451894
15	7.441699	0.007609	-0.007609	3.491670
16	5.235168	-0.007609	-0.007609	3.876166
17	4.968862	0.007609	-0.007609	3.922571
18	1.263411	-0.007609	-0.007609	4.568261
19	0.997106	0.007609	-0.007609	4.614665
20	0.122102	-0.007609	-0.007609	4.767138
21	0.000000	-0.007609	-0.007609	4.788415
22	-0.760873	-0.005016	-0.007609	4.921000
23	-0.780938	0.000000	0.014723	4.924496
24	-0.780938	0.000000	0.000000	3.340487
25	-0.780938	-0.002032	-0.005965	2.407411
26	-0.772809	-0.006133	0.012036	2.259317
27	-0.000008	-0.006133	0.006133	-5.940195
IMG	0.000000	-0.006133		-5.940283

(b) Refractive Zoom 10×

Figure 4.11: This figure shows two different zooms for the telescope. Here "HMY" stands for height of the marginal ray and "HCY" is the height of the chief ray. The height is tracked as it progresses past each surface, finally ending on the detector. Plot (a) shows the 1× zoom. Plot (b) shows an increase in the maginitude of the chief ray of 10×. This leads to a 10× larger image on the detector. The amount of zoom depends soley on the focal length ratios of the optics along each path. The height of the marginal ray shows each image is in focus on the detector.

process. The amount of zoom achievable is dependant on the focal length ratio of the optics along each path.

4.3.2 Defocus.

The refractive zoom, unlike the previous design, does not need a large focus aberration. In order to avoid post-processing, focus-dependence as a function of field angle should be small. Also, no overall focus offset should be seen. This is clearly obvious in Fig. 4.12. Not all of the astigmatism has been worked out of this system, but optimization of the beam paths could minimize this. The 1× and 10× refractive zooms have nearly an order of magnitude less aberration than the previous method.

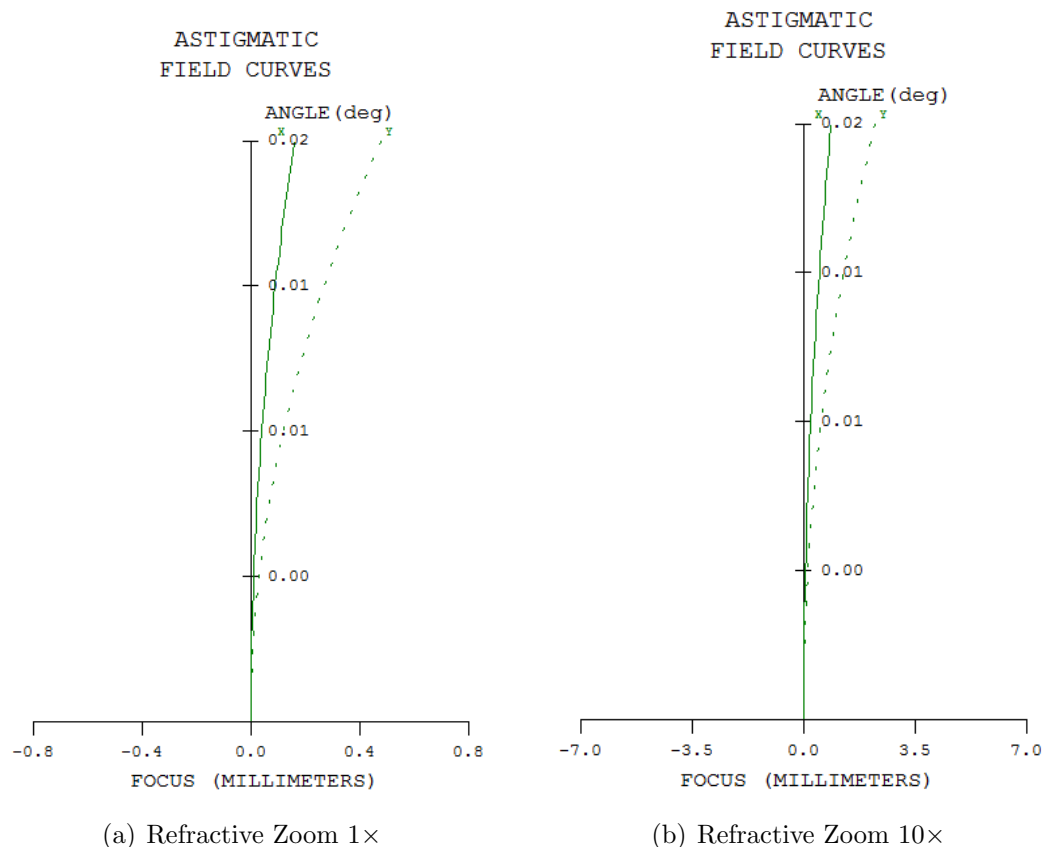(a) Refractive Zoom 1×   (b) Refractive Zoom 10×

Figure 4.12:   This figure shows two different zooms for the telescope. Plot (a) shows that the focus aberration as a function of field angle for the 1× refractive zoom path. Plot (b) shows the 10× refractive zoom path. The focus error for the 1× zoom is nearly an order of magnitude less than the in-focus beam of the prevous design. Plot (b) only has half of the focus error of the in-focus beam from the first design. Astigmatism over the field has not been removed completely, but optimization of the optics could reduce this.

As field angle increases, so does focus error. This is acceptable for small fields of view, but could cause wide field-of-view systems to need distortion correction. Plot (b)

4.3.3   Spot Diagrams.

An analysis of the spot diagrams shows that this system is well corrected for the 1× zoom path (see Fig. 4.13) compared to the previous design. The slightly different spot size for each wavelength is expected because the diameter is wavelength-dependent. As field angle increases, the spot gets more spread out from chromatic
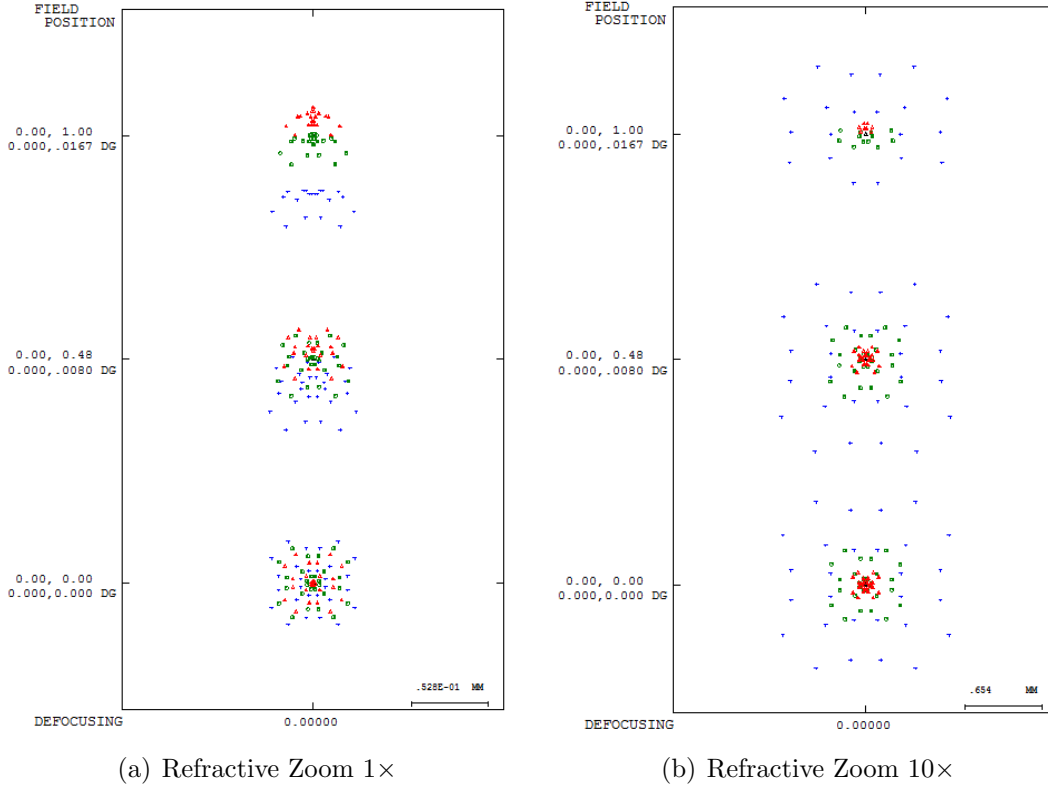
(a) Refractive Zoom 1× (b) Refractive Zoom 10×

Figure 4.13:   This figure shows spot diagrams for two different zooms of the tele-scope. The colors represent wavelengths of the d, c, f spectrum, and the three spots are shown at different field angles. Plot (a) shows that the 1× refractive zoom is producing a diffraction-limited spot. Further optimization could reduce this depen-dence and should be done if trying to build this system. Plot (b) shows the spot diagram for the 10× refractive zoom beam path. The increased zoom comes at the price of increasing spot size and chromatic aberration. Field angle dependence is quite obvious.

aberration in the system. The 10× zoom has a spot diagram that is much larger than the 1× and has more chromatic aberration, but this is the trade for the increased optical zoom.

4.3.4   Point Spread Function.

An analysis of the point spread functions shows agreement with the findings from the spot diagrams. The PSF for the 1× refractive zoom has a nice, diffraction-limited pattern (see Fig. 4.14). Ideally, the spot for the 10× refractive zoom would be shaped nearly the same way. Astigmatism in the path, though is causing the spot

56

to be flattened in one direction. An optimization of the optics and correction from the LC SLM could reduce the size greatly. If using the LC SLM, knowing the exact amount of aberration is not even necessary if the image entropy approach described in chapter 2 is used. As with the previous method, a slight field angle dependence on the PSF is observed.

4.3.5   Third-Order Aberrations.

Third-order aberrations break down the different deviations seen in the beam. As expected, spherical aberration plays a large role. This is due to using simple surfaces. The next most-prevalent aberrations for the $1\times$ and $10\times$ refractive zooms are astigmatism and coma, although they are an order of magnitude lower than spherical (see Fig. 4.15). Both of these could be reduced with optic optimization and LC SLM correction. A quick and simple analysis to do is called a ray aberration plot. These plots (see Fig. 4.16) confirm previous results and show spherical aberration and astigmatism. The $10\times$ refractive zoom image shows even larger aberration and astigmatism. In order to show the large reduction in overall aberrations using this method, Fig. 4.17 is plotted on the same scale as the ray aberrations for the previous method. Even at large optical zoom, total aberrations using the refractive zoom are much smaller than the method of post-processing.
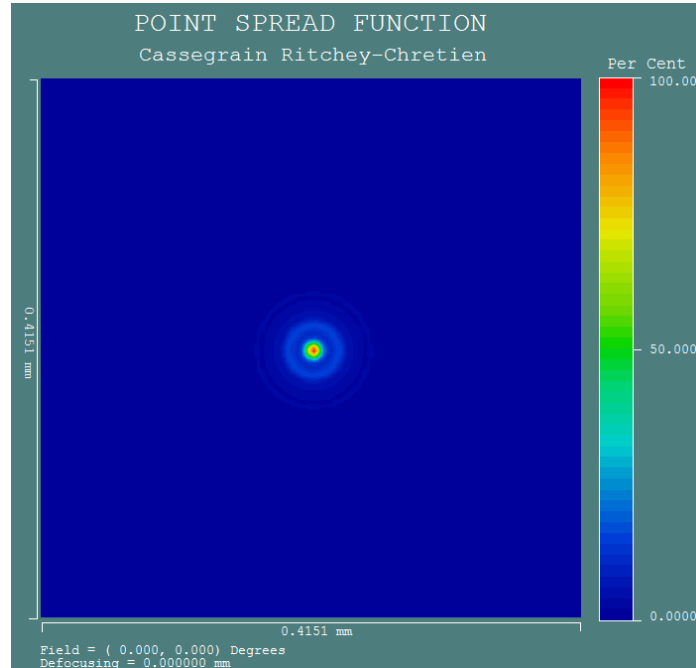
(a) Refractive Zoom 1×, Field Angle 0.0 deg
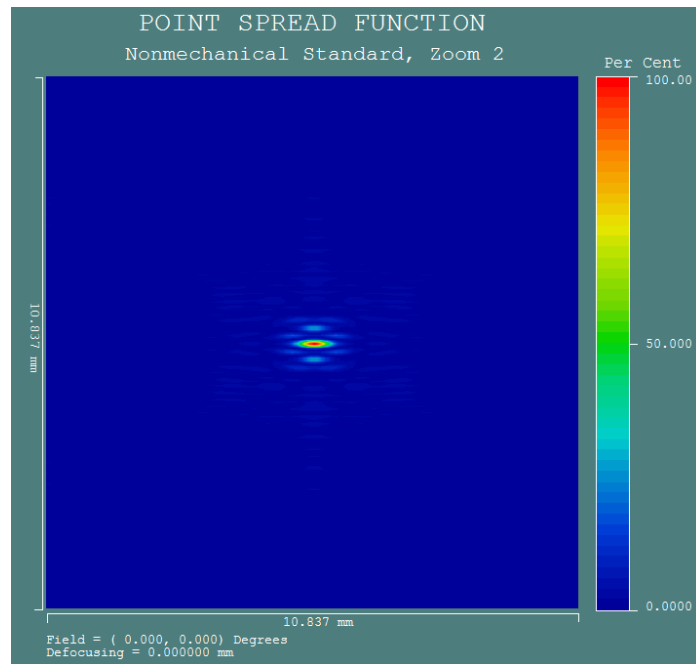
(b) Refractive Zoom 10×, Field Angle 0.0 deg

Figure 4.14: This figure PSFs for two different zooms of the telescope. Plot (a) shows the PSF for the refractive zoom 1× path for the on-axis field. Plot (b) shows the PSF for the refractive zoom 10× path for the on-axis field. Limitations of system memory prevented proper sampling the 10× zoom PSF. A more powerful computing machine could be used to accurately model this path.

```
        SA         TCO        TAS        SAS        PTB        DST        AX         LAT        PTZ
STO  -9.872296   0.051305  -0.000059   0.000000   0.000030   0.000000   0.000000   0.000000   0.002692
     10.329851   0.000000   0.000000   0.000000              0.000000  ASPHERIC CONTRIBUTIONS
  2   3.452889  -0.027611  -0.000002  -0.000051  -0.000076   0.000000   0.000000   0.000000  -0.006891
     -3.910514  -0.023706  -0.000048  -0.000016              0.000000  ASPHERIC CONTRIBUTIONS
  3   0.000000   0.000000   0.000000   0.000000   0.000000   0.000000   0.000000   0.000000   0.000000
  4   0.261151   0.023215   0.000762   0.000303   0.000074   0.000009   0.154954   0.004592   0.006704
  5   0.000000   0.000000   0.000000   0.000000   0.000000   0.000004   0.000000   0.003207   0.000000
  6   0.000000   0.000000   0.000000   0.000000   0.000000   0.000000   0.000000   0.000000   0.000000
  7   0.000000   0.000000   0.000000   0.000000   0.000000   0.000000   0.000000   0.000000   0.000000
  8   0.000000   0.000000   0.000000   0.000000   0.000000   0.000000   0.000000   0.000000   0.000000
  9   0.000000   0.000000   0.000000   0.000000   0.000000   0.000000   0.000000   0.000000   0.000000
 10   0.000000   0.000000   0.000000   0.000000   0.000000   0.000000   0.000000   0.000000   0.000000
 11   0.000000   0.000000   0.000000   0.000000   0.000000   0.000000   0.000000   0.000000   0.000000
 12   0.000000   0.000000   0.000000   0.000000   0.000000   0.000000   0.000000   0.000000   0.000000
 13   0.000000   0.000000   0.000000   0.000000   0.000000   0.000000   0.000000   0.000000   0.000000
 14   0.000000   0.000000   0.000000   0.000000   0.000000   0.000000   0.000000   0.000000   0.000000
 15   0.000000   0.000000   0.000000   0.000000   0.000000   0.000000   0.000000   0.000000   0.000000
 16  -0.002887  -0.005023  -0.002941  -0.001000  -0.000029  -0.000580  -0.039660  -0.023001  -0.002602
 17  -0.041611  -0.057451  -0.026469  -0.008842  -0.000029  -0.004069  -0.079194  -0.036447  -0.002602
 18   0.000000   0.000000   0.000000   0.000000   0.000000   0.000000   0.000000   0.000000   0.000000

SUM   0.216584  -0.039270  -0.028758  -0.009606  -0.000030  -0.004636   0.036100  -0.051648  -0.002700
```

(a) Third Order Ab. 1× Zoom

```
        SA         TCO        TAS        SAS        PTB        DST        AX         LAT        PTZ
STO  97.087381  -0.504551   0.000583   0.000000  -0.000291   0.000000   0.000000   0.000000   0.002692
   -101.587134   0.000000   0.000000   0.000000              0.000000  ASPHERIC CONTRIBUTIONS
  2 -33.956839   0.271535   0.000022   0.000504   0.000746  -0.000001   0.000000   0.000000  -0.006891
     38.457270   0.233130   0.000471   0.000157              0.000000  ASPHERIC CONTRIBUTIONS
  3   0.000000   0.000000   0.000000   0.000000   0.000000   0.000000   0.000000   0.000000   0.000000
  4  -2.568245  -0.228303  -0.007490  -0.002980  -0.000725  -0.000088  -1.523868  -0.045155   0.006704
  5   0.000000   0.000000   0.000000   0.000000   0.000000  -0.000038   0.000000  -0.031542   0.000000
  6   0.000000   0.000000   0.000000   0.000000   0.000000   0.000000   0.000000   0.000000   0.000000
  7   0.000000   0.000000   0.000000   0.000000   0.000000   0.000000   0.000000   0.000000   0.000000
  8   0.000000   0.000000   0.000000   0.000000   0.000000   0.000000   0.000000   0.000000   0.000000
  9   0.000000   0.000000   0.000000   0.000000   0.000000   0.000000   0.000000   0.000000   0.000000
 10   0.000000   0.000000   0.000000   0.000000   0.000000   0.000000   0.000000   0.000000   0.000000
 11   0.000000   0.000000   0.000000   0.000000   0.000000   0.000000   0.000000   0.000000   0.000000
 12   0.000000   0.000000   0.000000   0.000000   0.000000   0.000000   0.000000   0.000000   0.000000
 13   0.000056   0.000184   0.000237   0.000102   0.000035   0.000112   0.048977   0.053504  -0.000327
 14   0.000834   0.000332   0.000079   0.000050   0.000035   0.000007   0.099372   0.013181  -0.000327
 15   0.000000   0.000000   0.000000   0.000000   0.000000   0.000000   0.000000   0.000000   0.000000
 16   0.000000   0.000000   0.000000   0.000000   0.000000   0.000000   0.000000   0.000000   0.000000
 17   0.000000   0.000000   0.000000   0.000000   0.000000   0.000000   0.000000   0.000000   0.000000
 18   0.000000   0.000000   0.000000   0.000000   0.000000   0.000000   0.000000   0.000000   0.000000
 19   0.000000   0.000000   0.000000   0.000000   0.000000   0.000000   0.000000   0.000000   0.000000
 20   0.000000   0.000000   0.000000   0.000000   0.000000   0.000000   0.000000   0.000000   0.000000
 21   0.000000   0.000000   0.000000   0.000000   0.000000   0.000000   0.000000   0.000000   0.000000
 22   0.000015  -0.000008   0.000001   0.000000   0.000000   0.000000   0.005012  -0.000873   0.000000
 23   0.000046  -0.001297   0.012986   0.004792   0.000695  -0.045403   0.009954  -0.094309  -0.006423
 24   0.000000   0.000000   0.000000   0.000000   0.000000   0.000000   0.000000   0.000000   0.000000
 25   0.000003   0.000043   0.000486   0.000350   0.000282   0.001657   0.004033   0.019110  -0.002602
 26   0.000044  -0.000898   0.006423   0.002329   0.000282  -0.015929   0.008053  -0.055084  -0.002602
 27   0.000000   0.000000   0.000000   0.000000   0.000000   0.000000   0.000000   0.000000   0.000000

SUM  -2.566568  -0.229834   0.013797   0.005304   0.001058  -0.059683  -1.348468  -0.141169  -0.009777
```

(b) Third Order Ab. 10× Zoom

Figure 4.15: This figure shows the third-order aberrations for two zooms of the telescope. Plot (a) shows that the 1× refractive zoom is has very little aberration and has mainly spherical contributions. Plot (b) shows that the 10× refractive zoom has about an order of magnitude larger spherical (SA), coma (TCO), and astigmatism (TAS and SAS) aberrations. The total, though, is still small and may be partially corrected with image entropy analysis using the LC SLM.
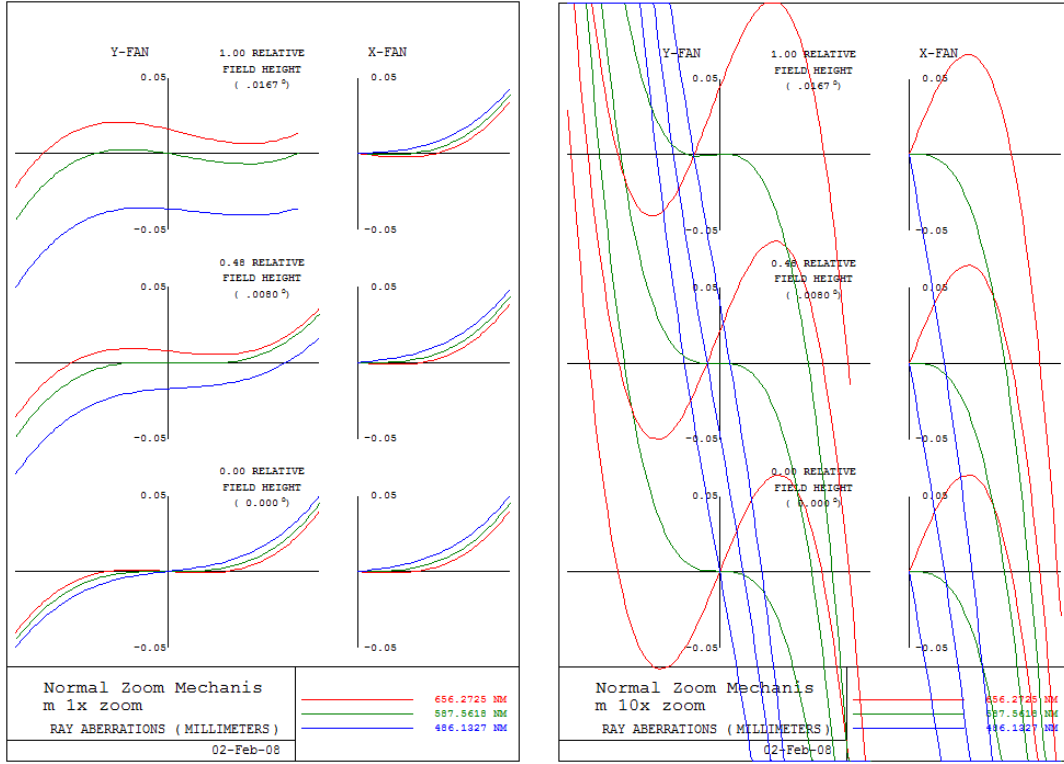
(a) Ray Aberration 1× Refractive Zoom

(b) Ray Aberration 10× Refractive Zoom

Figure 4.16: This figure shows ray aberration curves for two different zooms of the telescope. Ideally the curves would be flat. Curving up and down at the sides indicates spherical aberration. Tilting of the line across the origin indicates defocus. Diffrent focus tilts in the x and y fans indicate astigmatism. Plot (a) shows the curves for the 1× refractive zoom. Astigmatism is very small for all field angles. Spherical aberration is present in all cases. Plot (b) shows the the curves for the 10× refractive zoom. Larger spherical aberration and defocus are prevalent at every field angle.
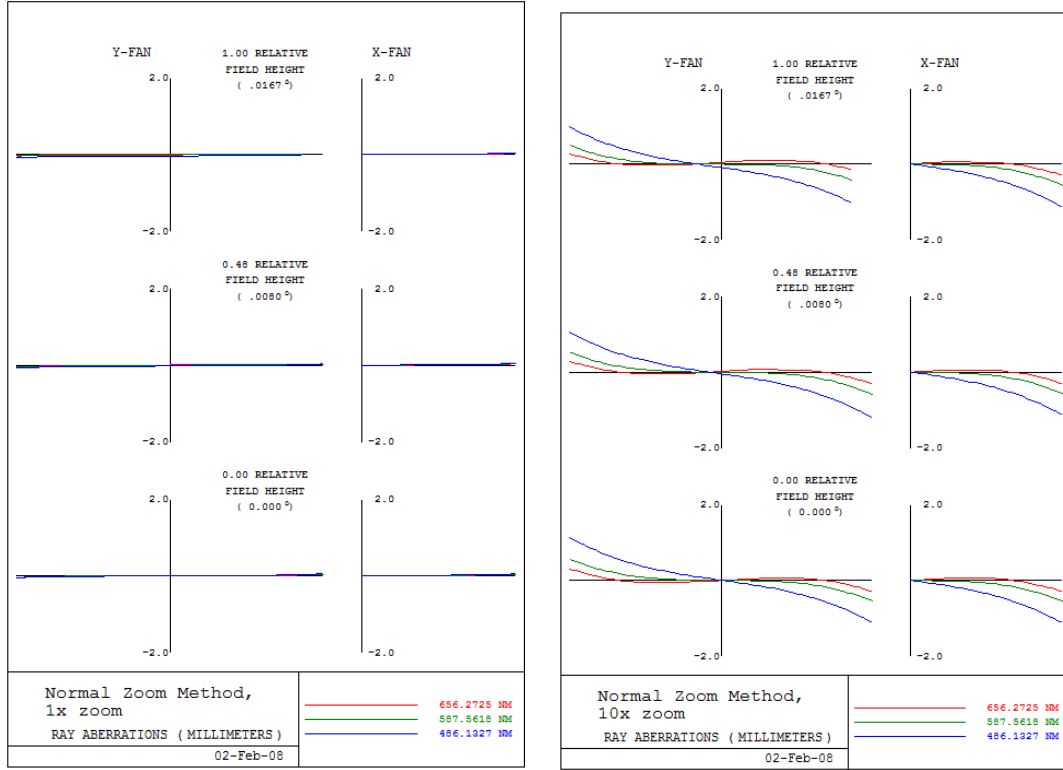
(a) Ray Aberration 1× Refractive Zoom   (b) Ray Aberration 10× Refractive Zoom

Figure 4.17:   This figure shows ray aberration curves from Fig. 4.16 plotted on the same scale as Fig. 4.6. Even at large optical zoom, total aberrations using refractive zoom are much smaller than the method of post-processing.

V. Conclusions, Impact, and Suggestions

This chapter will draw conclusions from results presented in the research. The potential impact of a nonmechanical zoom telescope on certain areas of concern to the United States Air Force mission is also explored. Finally, suggestions and guidelines are given for possible future work in this area.

5.1 Conclusions

As of this date, a nonmechanical, multi-path zoom telescope has not been built. The only previous research done has 2 possible paths, a very limited range on possible zooms, and relies on an unproven optical switch technology. This research shows a four-path nonmechanical zoom telescope that can have four seperate optical zoom subregions. Only proven components and technology are utilized to achieve this.

Not only is a multi-path nonmechanical zoom telescope possible, but it can have several desireable features. It can be made to be extremely compact, with all components fitting in a 24" × 18" × 18" box. This could easily fit on the back of a telescope, without need for a coudè path. All compenents can be bought or made using inexpensive, small optical surfaces - most or all of which can be found in commercial-off-the-shelf catalogs. The design is extremely scalable, and can be made larger if necessary. Also, over 90 percent of the incoming light can be sent down each path. To save even more cost, recombination of the seperate paths means only one detector is necessary.

To greatly reduce the number of optical components and alignment complexity, light from each path does not need to be focused in the image plane. A single curved mirror along each path, each with different focal lengths, can create large and out-of-focus images. The focus aberration can be removed with post-processing using a Richardson-Lucy iterative deconvolution algorithm. This method showed that zooms of up to a 3× magnification are easily achieveable. This was shown by tracking the height of the chief rays through the system for different beam paths. Marginal ray

height confirms that the 3× magnification image is nowhere near focus. A deeper look at defocus showed a large magnitude, and nearly constant focus offset.

Optimization of the optics needs to be done before building this version. A spot in the image plane for the in-focus leg was not diffraction-limited. The other beam paths, once focus is corrected, would most likely incur an even larger deviation from the diffraction limit. Spot diagrams showed that a large field-angle dependency as well as some chromatic aberration exists. PSFs for the out-of-focus paths were extremely difficult to compute due to the large grid size needed to accurately represent the wavefront in the image plane. Even with these difficulties, initial simulations with three-bar patterns make this a promising and viable possibility.

Using a LC SLM has several key beneficial effects on the system. Most importantly, it is the root of the nonmechanical beam path selection process. The small variations in reflected angle get magnified in a four mirror sytem. After the four mirrors, light will propagate to one of four sides of an optical pyramid. Each side goes to a different beam path. Light from each leg is redirected towards the image plane. The second significant effect it has is system aberration correction. Using inexpensive optical components can introduce up to 10 waves of spherical aberration - the most dominant aberration by an order of magnitude. The LC SLM has no problem correcting up to 40 waves, so it will not be challenged with its dynamic range. The process of image entropy could be used to determine preset LC SLM positions of lowest aberration for each path. The determined presets can easily be broken down into zernike polynomials and stored as calibrations. Such polynomials can be electronically sent to the LC SLM to fit whatever path is desired.

There are multiple drawbacks of using a LC SLM. First, the images will have to be bandpass limited due to the nature of the LC SLM using index of refraction change for control. While this can be over100 nm, it does represent a serious restriction. Secondly, the LC SLM will impart a diffraction efficiency. This comes from the modulo 2π approximation of the wavefront. The minute space between pixels and

63

stair-step difference between each part has been experimentally shown to cause a light loss of several percent. Losing light in a telescope system is never desired, but the corrective capabilities make it worthwhile.

Using a standard refractive zoom process, it is possible to achieve four different optical zooms without the need to defocus the data. Larger zooms are realizable because light is not lost by making the image larger than the detector. The angle selection process is identical as before, but two lenses along each path are placed a distance apart equal to the sum of their focal lengths. The ratio of their focal lengths determines the amount of magnification in the image plane. Optical magnication in the image plane means increased spatial resolution, which is the same as an optical zoom.

Errors and aberrations for this design are significantly lower than for the setup that needs post-processing. Third order aberrations in the system were greatly reduced - up to an order of magnitude for some. The spot diagrams and PSFs show that for low field angle, diffraction-limited imaging can be achieved. Slight astigmatism does exist, but an optimization of the optics or LC SLM correction could help reduce this significantly.

5.2   Impact of Research

The scalability of this system makes it of potential use to the USAF on several fronts. The most obvious is satellite imaging. Currently the USAF does imaging of satellites using large telescopes and adaptive optical systems. Satellites, however, come in quite a variety of shapes and sizes. Also, satellites close enough to resolve tend to move quickly across the sky. There is no current, easy way to size a sensor perfectly for every pass. If the satellite does not fill the sensor, being able to near-instantly change the optical zoom without having to align or move anything mechanically could prove highly beneficial. An exaggerated example of this can be seen in Figure 5.1.

Increased resolution could be achieved with or without the need for post-proceessing. Keeping focus aberration in the data greatly reduces the number of optics, so this may
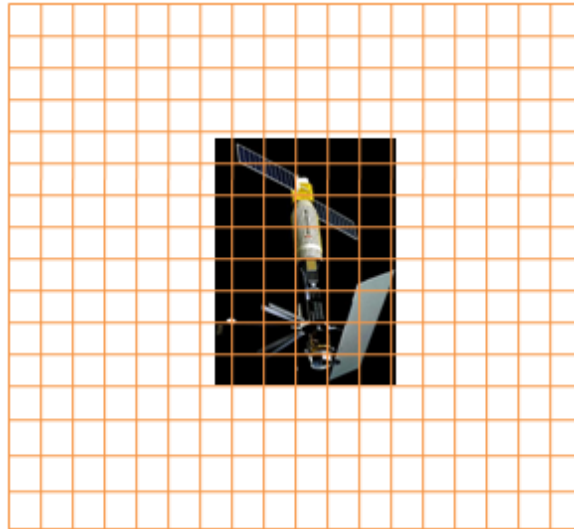
(a) Not Zoomed
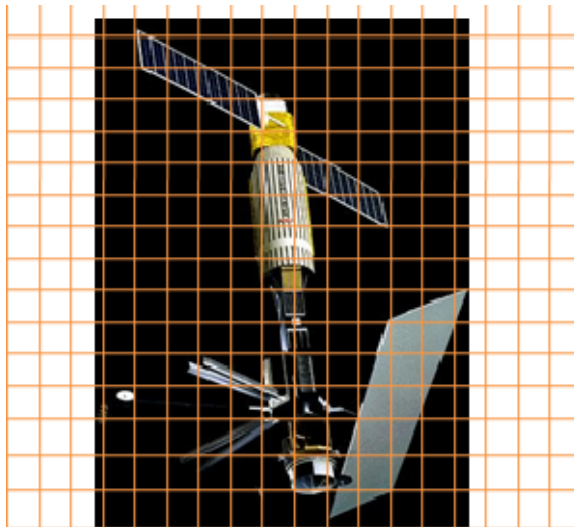
(b) Zoomed

Figure 5.1:   Being able to near-instantly magnify an image without moving any parts could prove very useful for imaging satellites. This is not to scale, but the orange grid represents the CCD. In plot (a), the satellite is smaller than the image plane. In plot (b), the satellite has been magnified, and spatial resolution has geen increased.

be an optimal choice for situations where weight is a constraint. Using the refractive zoom setup would be ideal if a clear image is desired without post-processing. Either choice could greatly reduce the risk of adding zoom to a system while potentially decreasing cost over a cam-driven motor. The absence of moving parts may also increase the lifetime of a system.

5.3   Suggestions for Future Work

The LC SLM is a key component to the nonmechanical zoom telescope. As discussed earlier, the process of image entropy can greatly reduce aberration from the system. A relationship between the best image and zernike polynomials needed across the LC SLM must be found. Minimizing aberrations this way keeps the cost of optical components low. Ideally, this process could be automated for each beam path. If successful, then a low-energy, self-calibration technique will have been found. An added bonus to this is that slight shifts in the optics will not matter - only the determined calibration.

The exact effect of light lost from the focus-correction method should be determined. As the PSF increases with increasing chief ray height from the optical axis, more information is lost from the edges. In addition, information that should not be on the detector will fall on the edges. This will limit the maximum zoom possible using this method and may effect the size of the detector chosen.

This design used only generic, large bandpass, optics and coatings. Careful consideration must be given to these details so that they are appropriate for the desired range of wavelengths. Likely, the amount of aberration in the system could be decreased significantly if an optimization on the chosen surfaces was performed. The size and curvature of each lens must also be matched to the size of the chosen image plane. This research did not put a restraint on image plane size to keep the design flexible, but this must be fully considered before constructing it.

If a broadband range is desired, free of diffractive losses, then it could be that a low-mechanical system may be a better choice. The LC SLM could be replaced with controllable turning flat. Obviously, this would not be a purely nonmechanical system, but it could provide a significant risk reduction over a typical zoom system.

Finally, the system needs to be set up in a laboratory to fully investigate the focus correction algorithm. A study of the retrieved image quality using post-processing versus the in-focus refractive zoom should be performed. This would establish a guideline for determining which type of optical zoom may be the best suited to the USAF mission.

Bibliography

1. Bagwell, Bret E., David V. Wick, Robert Batchko, Justin D. Mansell, Ty Martinez, Sergio R. Restaino, Don M. Payne, Jamie Harriman, Steve Serati, Gary Sharp, and Jim Schwiegerling. "Liquid Crystal Based Active Optics". *SPIE*, 6289:0801–0812, 2006.

2. ten Brummelaar, T.A. "Modeling atmospheric wave aberrations and astronomical instrumentation using the polynomials of zernike". *Optics Communication*, 132, 1996.

3. David M. Strong, Stephen C. Cain. "Maximum-a-priori (MAP) estimation of focus aberration in imaging systems". *Optical Engineering*, 46(12), Dec 2007.

4. Goodman, Joseph W. *Statistical Optics*. John Wiley & Sons, Inc., New York, NY, first edition, 1985.

5. Goodman, Joseph W. *Introduction to Fourier Optics*. McGraw Hill, New York, NY, second edition, 1996.

6. Hecht, Eugene. *Optics*. Addison Wesley, San Francisco, CA, fourth edition, 2002.

7. Linghua Guo, Zhaojun Liu Xiaoqing Ding Maofa Fang, Aimin Jiang. "Minimum Entropy for the Space Solar Telescope Automatic Focus". *SPIE*, 5642, 2005.

8. Lundgren, Mark A. "Multiple Field of View Telescope". *United States Patent*, US 6,765,719, 2004.

9. M. B. Garvin, R.C. Dymale J.R. Rotge, M.T. Gruneisen. "Image entropy as a metric for iterative optimization of large aberrations". *SPIE*, 5894:297–305, 2005.

10. Morrison, Fraknoi, Wolff. *Abell's Exploration of the Universe*. Saunders College Publsishing, Chicago, IL, seventh edition, 1995.

11. M.T. Gruneisen, J.R. Rotge Lewis F. DeSandre Donald L. Lubin, R.C. Dymale. "Compensated telescope system with programmable diffractive optic". *Optical Engineering*, 44(2), February 2005.

12. M.T. Gruneisen, J.R. Rotge R.C. Dymale Donald L. Lubin, Lewis F. DeSandre. "Programmable diffractive optics for wide-dynamic-range wavefront control using liquid-crystal spatial light modulators". *Optical Engineering*, 43(6):1387–1393, June 2004.

13. M.T. Gruneisen, J.R. Rotge R.C. Dymale Donald L. Lubin, Lewis F. DeSandre. "Wavelength-dependent characteristics of a telescope system with diffractive wavefront compensation". *Optical Engineering*, 44(6), June 2005.

14. M.T. Gruneisen, M. B. Garvin, R.C. Dymale. "Analysis of wavelegnth-dependences associated with modulo-Nλ_0 optical path control". *SPIE*, 5894:328–337, 2005.

15. M.T. Gruneisen, R.C. Dymale J.R. Rotge, M. B. Garvin. "Agile-field telescope system with diffractive savefront control". *SPIE*, 5894:345–350, 2005.

16. Schmidt, Jason D. *Free-Space Optical Communications Performance Enhancement by Use of a Single Adaptive Optics Correcting Element.* Ph.D. thesis, University of Dayton, 2006.

17. Steven C. Gustafson, John S. Loomis Gordon R. Little, Troy A. Rhoadarmer. "Smart Zooming". *SPIE*, 2238:170–175, 1994.

18. T. Poggio, F. Girosi. "Networks for Approximation and Learning". *IEEE*, 78:1481–1497, 1990.

19. Tyson, Robert. *Principles of Adaptive Optics.* Academic Press, Boston, MA, first edition, 1991.

20. W.H. Press, W.T. Vetterling B.P. Flannery, S.A. Teukolsky. *Numerical Recipes in C: The Art of Scientific Computing.* Cambridge University Press, 1992.

21. W.H.Richardson. "Bayesian-based iterative method of image restoration". *Journal of the Optical Society of America*, 61, 1972.

22. Wyant, James C. *Basic Wavefront Aberration Theory for Optical Metrology.* Academic Press, Boston, MA, 1992.

Vita

Eric W. Thompson was born and raised in Evansville, Indiana, where he attended Reitz Memorial High School. He earned a Bachelor of Science in Astronomy and Astrophysics from Indiana University while graduating with both university and departamental honors as well as the Hollis and Grete Johnson award for outstanding research. After commissioning as a Second Lieutenant in the Air Force, he moved to the Starfire Optical Range at Kirtland AFB. He was promoted to First Lieutenant on the Isle of Maui and was accepted into the Air Force Institute of Technology where he was promoted to Captain and pursued his Masters of Science in Electro-Optics.

Permanent address: 2950 Hobson Way
Air Force Institute of Technology
Wright-Patterson AFB, OH 45433

REPORT DOCUMENTATION PAGE

Form Approved
OMB No. 0704–0188

1. REPORT DATE *(DD–MM–YYYY)*	2. REPORT TYPE	3. DATES COVERED *(From — To)*
27–03–2008	Master's Thesis	Aug 2006 — Mar 2008

4. TITLE AND SUBTITLE

Nonmechanical Multizoom Telescope Design Using A
Liquid Crystal Spatial Light Modulator
and Focus-Correction Algorithm

5a. CONTRACT NUMBER

5b. GRANT NUMBER

5c. PROGRAM ELEMENT NUMBER

6. AUTHOR(S)

Thompson, Eric, W., Captain, USAF

5d. PROJECT NUMBER

ENP 08-295

5e. TASK NUMBER

5f. WORK UNIT NUMBER

7. PERFORMING ORGANIZATION NAME(S) AND ADDRESS(ES)

Air Force Institute of Technology
Graduate School of Engineering and Management (AFIT/EN)
2950 Hobson Way
WPAFB OH 45433-7765

8. PERFORMING ORGANIZATION REPORT NUMBER

AFIT/GEO/ENP/08-03

9. SPONSORING / MONITORING AGENCY NAME(S) AND ADDRESS(ES)

Mark T. Gruneisen, PhD
AFRL/RDSE
3550 Aberdeen Ave SE
Kirtland Air Force Base, NM 87117-5776
(505) 846-9298 (DSN: 246-9298), email: mark.gruneisen@kirtland.af.mil

10. SPONSOR/MONITOR'S ACRONYM(S)

11. SPONSOR/MONITOR'S REPORT NUMBER(S)

12. DISTRIBUTION / AVAILABILITY STATEMENT

Approved for public release; distribution is unlimited

13. SUPPLEMENTARY NOTES

14. ABSTRACT

Theoretical development and design of a compact nonmechanical multi-zoom telescope system is presented. A liquid crystal spatial light modulator (LC SLM) enables selection of four seperate beam paths without the use of moving parts. Each path incurs a different focus aberration in the image plane that can be deconvolved with postprocessing to yield four possible corrected magnification options. To increase flexibility, each region has a 40-wave subrange of focus. Optical zooms of up to 10 times magnification are feasible and are limited only by system noise and signal to noise ratio. Elimination of moving parts for focus could prove beneficial for sysems in which weight, volume, and power consumption have stringent requirements. The presented design can be constructed using all commercial off-the-shelf parts.

15. SUBJECT TERMS

nonmechanical zoom, telescope, spatial light modulator, deconvolution

16. SECURITY CLASSIFICATION OF:			17. LIMITATION OF ABSTRACT	18. NUMBER OF PAGES	19a. NAME OF RESPONSIBLE PERSON
a. REPORT	b. ABSTRACT	c. THIS PAGE			Jason D. Schmidt, Capt, USAF (ENG)
U	U	U	UU	81	**19b. TELEPHONE NUMBER** *(include area code)* (937) 255–3636, x7224 jschmidt@afit.edu

Standard Form 298 (Rev. 8–98)
Prescribed by ANSI Std. Z39.18